$BaBi_2O_6$: a Promising n-Type Thermoelectric Oxide with the $PbSb_2O_6$ Crystal Structure

Kieran B. Spooner[a],[†,‡] Alex M. Ganose[a],[¶,‡,§] W. W. Winnie Leung,[†] John Buckeridge,[‖,‡] Benjamin A. D. Williamson,[⊥] Robert G. Palgrave,[†] and David O. Scanlon[*,†,‡,§]

†*Department of Chemistry, University College London, 20 Gordon Street, London WC1H 0AJ, UK*

‡*Thomas Young Centre, University College London, Gower Street, London WC1E 6BT, UK*

¶*Department of Materials, Imperial College London, South Kensington Campus, London SW7 2AZ, UK*

§*Diamond Light Source Ltd., Diamond House, Harwell Science and Innovation Campus, Didcot, Oxfordshire OX11 0DE, UK*

‖*School of Engineering, London South Bank University, London SE1 0AA, UK*

⊥*Department of Materials Science and Engineering, Norwegian University of Science and Technology (NTNU), Trondheim 7491, Norway*

E-mail: d.scanlon@ucl.ac.uk

[a]These authors contributed equally to this work.

Abstract

Thermoelectric materials offer the possibility of enhanced energy efficiency due to waste heat scavenging. Based on their high temperature stability and ease of synthesis, efficient oxide-based thermoelectrics remain a tantalising research goal, however, their

current performance is significantly lower than the industry standards such as Bi_2Te_3 and PbTe. Among the oxide thermoelectrics studied thus far, the development of n-type thermoelectric oxides has fallen behind that of p-type oxides, primarily due to limitations on the overall dimensionless figure of merit, or ZT, by large lattice thermal conductivities. In this article, we propose a simple strategy based on chemical intuition to discover enhanced n-type oxide thermoelectrics. Using state-of-the-art calculations we demonstrate that the $PbSb_2O_6$-structured $BaBi_2O_6$ represents a novel structural motif for thermoelectric materials, with a predicted ZT of 0.17–0.19. We then suggest two methods to enhance the ZT up to 0.22, on par with the current best earth-abundant n-type thermoelectric at around 600K, $SrTiO_3$, which has been much more heavily researched. Our analysis of the factors that govern the electronic and phononic scattering in this system provides a blueprint for optimising ZT beyond the perfect crystal approximation.

Introduction

Society is facing ever increasing energy demands due to our inexorable dependence on technology, whilst urgently needing to stop global heating caused largely by the carbon emissions of those demands.[1] It is therefore imperative that we innovate in the area of renewable energy technologies, to ensure a sustainable climate for future generations. Thermoelectrics, materials that can generate a voltage driven by a temperature gradient, are especially interesting as 50 % of generated energy is wasted as heat.[2] They could therefore significantly reduce our energy demands by recycling some of this waste, on top of providing a new avenue for sustainable energy generation.

The efficiency of thermoelectric materials is quantified using the dimensionless figure of merit, $ZT = S^2\sigma T/(\kappa_{\text{ele}} + \kappa_{\text{lat}})$, where S is the Seebeck coefficient, σ is the electrical conductivity, T is the absolute temperature, and κ_{ele} and κ_{lat} are the electronic and lattice contributions to the thermal conductivity, respectively. Maximising ZT is not a simple task,

as there are a number of competing terms in the equation. As the electrical conductivity of a material is increased, so too necessarily is the electronic contribution to the thermal conductivity, as $\kappa_{\text{ele}} \approx L\sigma T$, where L is the Lorenz number.[3] Similarly, to achieve a high electrical conductivity, it is preferable to have a semiconductor with a reasonable dispersion of the band edges, so that charge carriers will have high mobility. Conversely, to achieve a high Seebeck coefficient, flatter (non-disperse) band edges are preferable, meaning that maximising the so-called power factor (given by $S^2\sigma$) is also problematic. Therefore strategies have evolved to try to find a "phonon-glass electron-crystal", i.e. a material that conducts electricity like a single crystal but conducts heat like an amorphous solid.[4]

In the past decade, research breakthroughs have seen lab-based thermoelectric materials punch through the $ZT = 2$ ceiling, however, these systems are normally based on compounds such as PbTe[5–9] or Bi_2Te_3[10] which contain rare or toxic elements. Earth abundant alternatives have been emerging, including SnSe which has yielded the highest ZT measured thus far of 2.6,[11] however widespread adoption of SnSe in industrial modules is still a long way off. Oxide thermoelectrics, which can be comprised of non-toxic elements, stable to high temperatures and stable in air, have been heavily studied since 1997, when Terasaki first reported a large thermopower in p-type Na_xCoO_2.[12] Over the past two decades, development of p-type oxide thermoelectrics has seen the maximum reported ZT rise to $\sim$1 for Na_xCoO_2 at 800 K in air in 2001,[13] and to 1.1 for $Bi_2Sr_2Co_2O_y$ at 973 K in air in 2002.[14] More recently, computational work on the mixed anion oxyphosphides LaZnOP and LaZnOAs have predicted p-type ZTs of 2.10 and 1.92 respectively at 1000 K,[15] although this is yet to be experimentally confirmed.

Efficient all oxide thermoelectric modules, however, need both p-type and n-type oxides with high figures of merit, and thus far the development of a high performance n-type thermoelectric oxide is the limiting factor.[16] Perovskite structured oxides such as $SrTiO_3$ and $CaMnO_3$ have received a large amount of attention, however the ZT for $SrTiO_3$ has only reached 0.37 at 1000 K with Nb doping;[16] while the ZT of $CaMnO_3$ based compounds

languishes at 0.2 for $Ca_{0.9}Dy_{0.1}MnO_3$ and $Ca_{0.9}Yb_{0.1}MnO_3$, both at 1000 K.[17] The limiting factor for both has been shown to be the large lattice thermal conductivity.[18,19] In fact a recent study by Daniels *et al.* used the concept of cation mutation to transform $SrTiO_3$ to $La_{0.5}Na_{0.5}TiO_3$ in an effort to reduce the lattice thermal conductivity.[20] This cation mutation successfully reduced the lattice thermal conductivity by 80 %, however the maximum ZT achieved for $La_{0.5}Na_{0.5}Ti_{0.8}Nb_{0.2}O_3$ peaked at 0.2 at about 800 K.

Another strategy for designing n-type thermoelectrics has been to test the materials currently used as transparent conducting oxides (TCOs), such as In_2O_3 and ZnO. These wide band gap oxides, which share an np^0 ns^0 electronic structure of the cation states, show high conductivities when donor doped. The np^0 ns^0 electronic structure yields a very dispersive conduction band, which ensure low effective masses of the charge carriers. This ensures a high electrical conductivity when degenerately doped, however the Seebeck coefficient is lower than that seen for p-type oxide thermoelectrics. ZTs for Al-doped ZnO have reached 0.3 at 1273 K,[21] whereas those for for Ge-doped In_2O_3 have reached 0.45 at 1273 K, which represents the champion ZT for a singly doped n-type oxide.[22] When dually doped with Ga and Al, ZnO reaches an even higher ZT of 0.65 at 1000 K.[23] A major limiting factor of the performance of these systems is the large lattice thermal conductivity, which has been computationally predicted to be due to long phonon mean free paths in several TCOs.[24] Indeed, the ZT of 0.45 for $In_{1.8}Ge_{0.2}O_3$ is only achievable as the solubility limit of Ge in $In_{2-x}Ge_xO_3$ is reached at $x = 0.2$, where the lattice thermal conductivity is reduced due to the presence of $In_2Ge_2O_7$ inclusions in the In_2O_3 matrix.[22]

It is instructive to note that materials with electronic structures similar to the known TCOs such as In_2O_3, ZnO, SnO_2, CdO and $BaSnO_3$ always display high electrical conductivity when donor doped.[25–31] A simple strategy to design new n-type thermoelectrics would therefore be to search for materials which possess cations with similar np^0 ns^0 electronic structures, with 3D or 2D connectivity of the metal–oxygen network (octahedra or tetrahedra) to ensure electrical transport pathways exists, however with more complex crystal

structures to ensure a lower lattice thermal conductivity. Ideally, these more complex structures would feature heavier elements to dampen the speed of the phonons.[32] Using these design criteria, we have selected Bi^{5+} containing compounds as being worthy of study, as Bi in the 5+ oxidation state possesses an np^0 ns^0 electronic structure, and Bi-based systems have been studied previously as potential thermoelectrics.[10,33–35]

In 2004, Mizoguchi and Woodward first synthesised $BaBi_2O_6$ by hydrothermal methods.[36] $BaBi_2O_6$ crystallises in a hexagonal $PbSb_2O_6$ structure (space group $P\bar{3}1m$ (162)), otherwise known as the rosiaite structure after the Rosia mine in Italy, where $PbSb_2O_6$ occurs naturally.[37] $BaBi_2O_6$ features two-dimensional layers of edge sharing BiO_6 octahedra, with two thirds of all the octahedral holes in the 2D-layer occupied, as demonstrated in Figure 1. The Ba cations sit between the BiO_6 layers situated directly above and below the unoccupied octahedral holes. Oxygen has distorted trigonal planar coordination with two Bi ions and one Ba ion. $BaBi_2O_6$ has been reported to have a band gap of 2.6 eV,[36] which

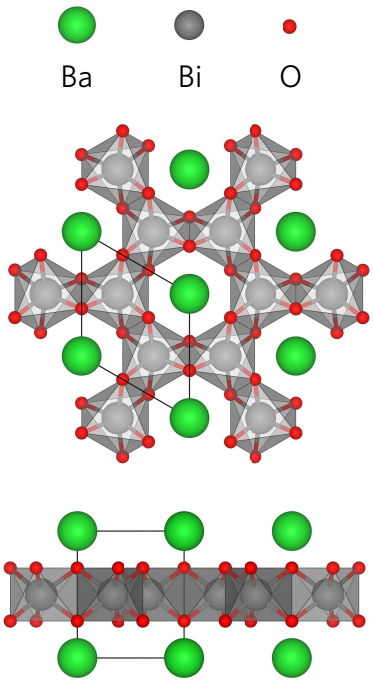

Figure 1: Crystal structure of $BaBi_2O_6$, highlight the layered nature (top) and the edge sharing BiO_6 octahedra. Ba, Bi, and O atoms are denoted by green, grey, and red spheres, respectively. Drawn with Vesta.[38]

along with the high dispersion in the conduction band has been attributed as the cause of its strong photocatalysis of phenol.[39] This high dispersion is also beneficial to thermoelectrics, which need to be conductive. The potential for high conductivity, combined with large mass differences that are expected to increase phonon scattering, make $BaBi_2O_6$ an attractive candidate for oxide thermoelectric applications.

Computational Methodology

The following calculations were conducted using density functional theory (DFT), using the Vienna *ab initio* Simulation Package (VASP)[40–43] with plane augmented-wave (PAW) pseudopotentials.[44] k-point and plane-wave energy convergence were tested on the 9 atom primitive cell, and a $3 \times 3 \times 3$ Γ-centred mesh and 400 eV cut-off found to converge the total energy to 10 meV atom^{-1} (ESI Figure S1). The structure was optimised so the force on each atom totalled less than 0.01 eV Å^{-1} and the total electronic energy converged to less than 1×10^{-5} eV, with a larger cut-off energy of 520 eV to avoid basis set errors arising from Pulay stress.[45] Geometry optimisations were performed using the HSE06 functional,[46] which is hybridised with 25 % Hartree–Fock exchange,[47,48] which is screened out at long range.

A band structure and density of states (DoS) were also calculated using the HSE06 functional, and these were then plotted with the sumo package.[49] The effective mass of the charge carriers at the band extrema were calculated by approximating the bands as parabolic and using the relationship:

$$\frac{1}{m^*_{ij}} = \frac{\delta^2 E(k)}{\delta k_i \delta k_j} \frac{1}{\hbar^2} \tag{1}$$

where $E(k)$ refers to the eigenvalue of the band at a the CBM or VBM and m^*_{ij} refers to the effective mass. In order to more directly compare our theoretical and experimental electron energies, the Gaussian–Lorentzian (Galore) code[50] was used to simulate the X-ray photoelectron spectra (XPS).

Electronic transport properties including the electrical conductivity, Seebeck coefficient

and the electronic contribution to the thermal conductivity, were calculated using the Boltzmann Transport Properties (BoltzTraP)[51] and AMSET packages.[52] In both codes, transport properties are obtained by solving the Boltzmann transport equation using the Onsager coefficients. The primary difference between the packages is that BoltzTraP assumes a constant relaxation time (CRT), in our calculations set to 1×10^{-14} s, whereas AMSET explicitly calculates the scattering rate for each temperature, doping concentration, band and k-point. Accordingly, AMSET is able to provide insight into the fundamental scattering processes that limit charge transport and has demonstrated considerably improved agreement with experimental measurements of mobility in a range of semiconductors. AMSET includes scattering due to acoustic deformation potentials (ADP), piezoelectric interactions (PIE), polar optical phonons (POP), and ionised impurities (IMP). A maximum mean free path (MFP) of electrons can also be imposed to simulate nanostructuring. One benefit of AMSET compared to the state-of-the-art density functional perturbation theory combined with Wannier interpolation approach (DFPT+Wannier)[53] is that the scattering rates can be computed only using common materials parameters without the need for expensive DFPT calculations. The materials parameters and additional settings used in the AMSET calculations are provided in Table S3 of the ESI. The AMSET methodology, including the form of all scattering matrix elements, is given in detail in Ref. 52.

High lattice thermal conductivities have thus far limited the achievable ZTs for the existing n-type oxide thermoelectrics.[16,24] With the advent of increased computational power, it has become possible to directly compute many-phonon interactions from *ab initio* calculations, although this comes at considerable computational cost.[32] To provide accurate ZT predictions, however, we must pay this computational cost to quantify the lattice thermal conductivity, which can be plugged into the $ZT = S^2\sigma T/(\kappa_{\text{ele}} + \kappa_{\text{lat}})$ formula. In this study we employ the Phonopy[54] and Phono3py[55] packages, which use a finite-difference supercell approach to calculate the second- and third-order force constants and obtain the lattice thermal conductivity. In our calculations, we used a displacement distance of 0.01 Å for second

order force constants in Phonopy, and 0.03 Å for the second and third order force constants in Phono3py. Phonopy was used to check visually for convergence of the phonon dispersion relation with supercell size. For the second-order force constant calculations in Phono3py, a $4 \times 4 \times 4$ supercell was selected, and for the third-order force constants a $2 \times 2 \times 2$ supercell was selected. As the third-order force constants alone require 2216 calculations on a 72-atom supercell, we compute these interactions at the PBEsol level. PBEsol has been shown to be an excellent compromise between computational cost and accuracy for lattice dynamics calculations.[56] Forces were converged to a criterion of $1 \times 10^{-4}\,\mathrm{eV\,\AA^{-1}}$ and the electronic wavefunction converged to $1 \times 10^{-8}\,\mathrm{eV}$. Phonon transport properties were obtained using Phono3py by solving the Boltzmann transport equations under the single-mode relaxation time approximation where each mode is treated as if the rest are at equilibrium. The non-analytical correction (NAC) was also included, to take into account the charges on the ions.[57] The resulting lattice thermal conductivities were converged against q-point mesh (q-points are the lattice dynamics equivalent of k-points, where $\mathbf{q} = 2\pi\mathbf{k}$; convergence can be seen in ESI Figure S2). Furthermore, to investigate nanostructuring we used the boundary mean free path (BMFP) method in Phono3py, which constrains the lifetimes of phonons such that their maximum mean free path does not exceed a cut-off value (set to 20 nm in this work).

Defects were calculated in a $2 \times 2 \times 2$ (72 atom) supercell using the HSE06 functional, with a $2 \times 2 \times 2$ Γ-centred k-point mesh. The formation energy, ΔH_f, of a defect, D, with charge state, q, was calculated as:

$$\begin{aligned} \Delta H_{\mathrm{f}}^{D,q} = \left(E^{D,q} - E^{\mathrm{H}}\right) + \sum \left\{n_i(E_i + \mu_i)\right\} \\ + q\left(E_{\mathrm{F}} + \epsilon_{\mathrm{v}}^{\mathrm{H}}\right) + E_{\mathrm{corr}} \end{aligned} \tag{2}$$

where $E^{D,q}$ is the energy of the defective supercell and E^{H} is the energy of the host supercell.[58,59] The second term represents the energy change due to the exchange of an atom, i, with a chemical reservoir: n_i is the number of atoms of each type exchanged, E_i is the

element reference energy calculated from the element in its standard state, and μ_i is the chemical potential of the atom. $\epsilon_{\mathrm{v}}^{\mathrm{H}}$ represents the energy needed to add or remove an electron from the VBM to a Fermi reservoir — i.e. the eigenvalue of the VBM in the host — and E_{F} is the Fermi level relative to $\epsilon_{\mathrm{v}}^{\mathrm{H}}$. E_{corr} is a correction applied to account for various limitations of the defect scheme used and is comprised of three terms:

$$E_{\mathrm{corr}} = E_{\mathrm{potal}} + E_{\mathrm{bf}} + E_{\mathrm{icc}} \tag{3}$$

where E_{potal} is a correction to align the electrostatic potential of the defected supercell to that of the host,[58,60] E_{bf} corrects the effects on the total energy of erroneous band filling,[58] and E_{icc} accounts for the unphysical defect–defect Coulombic interactions that occur between periodic images of charged defects due to finite supercell size effects.[61]

The thermodynamic transition level, $\epsilon(D, q/q')$, defined as the energy at which the charge state of defect, D, spontaneously transforms from $q \leftrightarrow q'$, was calculated according to:

$$\epsilon(D, q/q') = \frac{E^{D,q} - E^{D,q'}}{q' - q} \tag{4}$$

The thermodynamic transition levels indicate whether a defect will act as a shallow or deep defect and can be measured experimentally through techniques such as deep-level transient spectroscopy.[59] The self-consistent Fermi level and defect concentrations were calculated using the SC-Fermi code.[62–65]

Experimental Methodology

Synthesis

Synthesis

Synthesis

All reagents were obtained from Sigma Aldrich in the highest purity available and used as received. $NaBiO_3$ was synthesised by adapting the method of Pan et al.[66] $Bi(NO_3)_3 \cdot 9\,H_2O$ (10.025 g, 18.00 mmol) was dissolved in 20 cm^3 1 M HNO_3 solution. 1 cm^3 of this $Bi(NO_3)_3$ solution was added to 20 cm^3 15 M NaOH solution and a white precipitate of $Bi(OH)_3$ formed immediately in the mixture. The precipitate was filtered, washed with deionised water and dried under vacuum. $Bi(OH)_3$ (2.239 g, 8.61 mmol) was added to 28 cm^3 10 % aqueous NaClO solution and stirred for 30 min. NaOH solution (11 M, 29.6 cm^3) was added to the reaction mixture and stirred for three days. The mixture turned from reddish-brown to yellow upon stirring. The resulting yellow $NaBiO_3$ precipitate was filtered and washed with water.

$BaBiO_3$ was synthesised from the hydrothermal reaction of $NaBiO_3$ and $BaCl_2$. $BaCl_2$ (1.501 g, 6.15 mmol) of $BaCl_2 \cdot 2\,H_2O$ and $NaBiO_3$ (0.4307 g, 1.54 mmol) of were placed in a 40 mL Teflon-lined autoclave with atomic ratio of Ba:Bi being 4:1. The powders were placed in a Teflon lined autoclave with 18 cm^3 of deionised water, and heated to 90 °C at a rate of 2.5 °C min^{-1}, then held at that temperature for 48 h, before cooling at a rate of 10 °C min^{-1}. The resulting orange crystals were filtered and washed with deionised water and acetone, before drying at 150 °C in air to obtain $BaBi_2O_6$.

Characterisation

Powder X-ray diffraction (PXRD) data was collected on a STOE diffractometer in transmission geometry using monochromated Mo Kα radiation over the 2θ range of 2–40° with a step size of 0.5° at 20 s per step. Optical diffuse-reflectance spectroscopy was measured between 205–2000 nm with a step size of 1 nm using PerkinElmer Fourier Transform Lambda 950 UV–vis spectrophotometer equipped with an integrating sphere at ambient temperature.

X-ray photoelectron spectroscopy (XPS) was also performed using a Thermo Scientific Kα spectrometer utilising a 72 W Al Kα radiation. High resolution scans with a binding energy step size of 0.1 eV were used and *in situ* Ar ion etching was performed using a 2 keV Ar ion beam in a background Ar pressure of 2×10^{-7} mbar. The binding energy scale was corrected for charring by adjusting the adventitious C 1s peak to 284.8 eV.

Results

Geometry

In Table 1 we compare the experimental and calculated lattice parameters of $BaBi_2O_6$. Our experimental and HSE06 results are in excellent agreement with those of Mizoguchi *et al.*, while the PBEsol results deviate slightly. The experiment of Saiduzzaman *et al.* underestimates the c parameter relative to the other experiments and HSE06, being close instead to the PBEsol calculations both in the c parameter and O positions (Table 2).

Table 1: The lattice parameters of $BaBi_2O_6$ obtained from our experiment, the experiments of Mizoguchi *et al.*[36] and Saiduzzaman *et al.*[39] and our PBEsol and HSE06 calculations

(Å)	Experimental	PBEsol	HSE06	Mizoguchi[36]	Saiduzzaman[39]
a	5.576(4)	5.610	5.590	5.576(3)	5.575534(6)
c	5.789(7)	5.721	5.806	5.785(7)	5.7381(1)

The powder XRD pattern of the synthesised $BaBi_2O_6$ matches well with those from the literature. Taking these as a starting point, Rietveld refinement yielded a good fit to the experimental pattern, with lattice parameters very close to those previously reported (Table 1). No additional peaks were observed.

Thermogravimetric analysis (TGA) of $BaBi_2O_6$ (Figures 3 and 4) showed a loss in mass starting at around 100 °C which could be attributed to the loss of hydration of water in the sample, consistent with the findings of Mizoguchi *et al.*[36] The second loss in mass was seen at 340 °C possibly due to the decomposition of $BaBi_2O_6$. This is consistent with the TGA

Table 2: The atom positions in $BaBi_2O_6$ from the experiment of Saiduzzaman *et al.*[39] and our PBEsol and HSE06 calculations

	Atom	a	b	c
Saiduzzaman[39]	Ba	0	0	0
	Bi	1/3	2/3	1/2
	O	0.6191(7)	0	0.2938(6)
PBEsol	Ba	0	0	0
	Bi	1/3	2/3	1/2
	O	0.620	0	0.291
HSE06	Ba	0	0	0
	Bi	1/3	2/3	1/2
	O	0.618	0	0.298

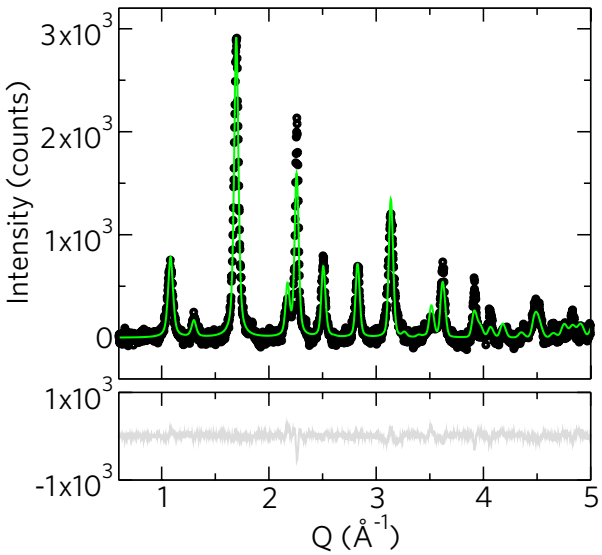

Figure 2: Powder X-ray diffraction patterns of $BaBi_2O_6$ as-synthesised (dots) and simulated (line). The experimental values were measured using a STOE diffractometer in transmission geometry using monochromated Mo Kα radiation.

of Saiduzzaman *et al.*, who attribute this loss to oxygen evolution and the accompanying reduction of Bi^{5+} to Bi^{3+}.[39] They then observe a mass gain, attributed to oxidation, which was not observed to a significant extent here, followed by another mass loss at 545 °C, once again attributed to oxygen evolution. Here, however, further decomposition of the sample did not occur until around 650 °C. Note that the small increase in mass between 20 °C and 100 °C was due to an instrument effect, in which a drift was created on the balance upon heating. The nature of these decompositions was studied by heating portions of $BaBi_2O_6$

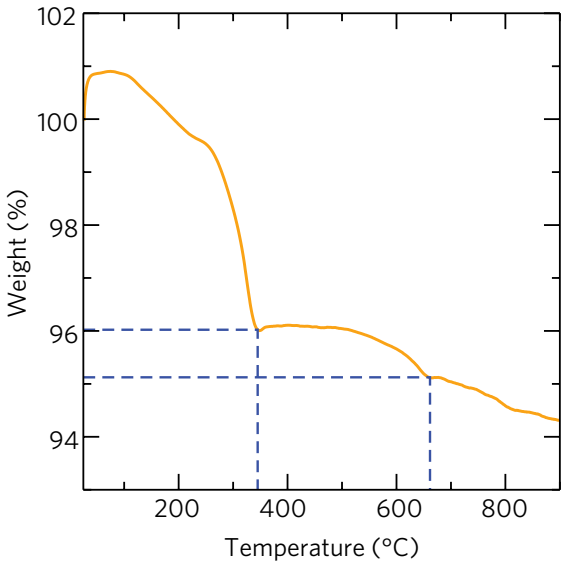

Figure 3: The thermogravimetric analysis of $BaBi_2O_6$ from 20 °C to 900 °C with machine artefact at low temperature.

to various temperatures, cooling and performing powder XRD measurements (Figure 3). The $BaBi_2O_6$ diffraction pattern is unchanged by heating the sample to 300°C, but changes significantly at 350°C and above, eventually at 600°C the pattern matches the perovskite $BaBiO_3$.

Electronic Structure

The HSE06-calculated total and partial electronic density of states (DoS) for $BaBi_2O_6$ are shown in Figure 5(a). As expected for a wide band gap oxide, the valence band is dominated

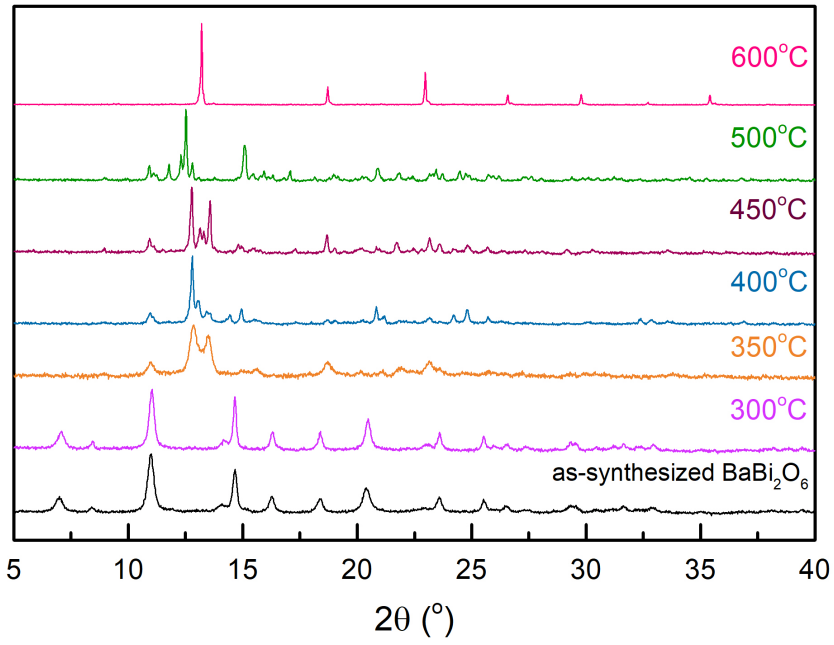

Figure 4: Powder X-ray diffraction patterns during heating of $BaBi_2O_6$ from 20 °C to 600 °C.

by O 2p states, with small contributions from Bi p and Bi 6s states near the top of the valence band. The conduction band minimum (CBM) is predominantly comprised of Bi 6s character with some minor O 2p contributions. The calculated band structure is shown in Figure 5(b). $BaBi_2O_6$ is a semiconductor with an indirect band gap of 2.87 eV along the Γ–M direction, although the direct band gap is only 2.90 eV at the Γ point. The efficient mixing between the Bi 6s and the O 2p states in the conduction band yield a large band width of 1.90 eV, which is indicative of high electron mobility. We have quantified this by calculating the effective masses at the CBM via parabolic band fitting in the sumo package;[49] the electron effective mass in the plane of the BiO_6 octahedra has a low value of 0.37 m_e, whereas perpendicular to the layers the effective mass is 0.53 m_e (Table 3). This dispersive lower conduction band indicates the possibility for high n-type conductivity if donor doping can be achieved.

We have verified the DoS results experimentally using X-ray photoelectron spectra, shown in Figure 6 together with the curve fitting as described in the previous section. The high

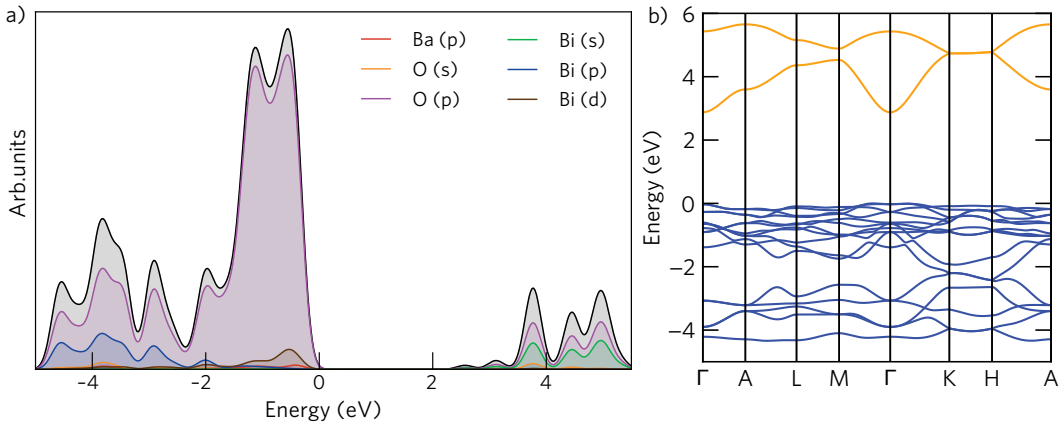

Figure 5: (a) density of states and (b) band structure of $BaBi_2O_6$ plotted with sumo.[49] In (b), the conduction band is in orange and the valence band in blue, with the valence band maximum set to 0 eV. The k-point path is using the Bradley–Cracknell formalism,[67] and the paths are shown in the Brillouin zone in ESI Figure S3.

Table 3: The effective masses of the charge carriers in $BaBi_2O_6$ from HSE06, calculated by parabolic band fitting in the sumo package.[49] The layers are in the ab plane.

Carrier	Direction	Effective mass (m_e)
e^-	a, b	0.368
e^-	c	0.527
h^+	a, b	1.351

resolution Ba $3d$ scan (Figure 6(a)) showed a spin-orbit doublet with an energy difference of 15.1 eV between the higher energy $3d_{3/2}$ and lower energy $3d_{5/2}$ components, which can be typically observed in barium oxide compounds.[68] Similarly, the spin-orbit doublet in the high resolution Bi $4f$ scan (Figure 6(b)) was composed of the lower energy component $4f_{7/2}$ at 158.7 eV and the higher energy component $4f_{5/2}$ at 164.0 eV, consistent with previous experiments.[69–75] Apart from the O $1s$ spectral component at 529.6 eV, there was an additional O $1s$ component within the region, which could be caused by the presence of hydroxide species (Figure 6(c)). The simulated and experimental valence band data shown in Figure 6(d) were in excellent agreement with the spectral peak at -4.9 eV corresponding to Bi $6s$ and p states. By adjusting the adventitious C $1s$ to 284.8 eV, the Fermi level was located at 0 eV on the valence band spectrum and the valence band edge was found to be 2.33 eV away from the Fermi level, indicating that the Fermi level was closer to the conduction band as predicted.

Diffuse reflectance data were transformed using Kubelka–Munk function[76] and Figure 7 shows the plots of $F(\mathrm{R})$ and $F(\mathrm{R})^2$ against energy using the Poeppelmeier method,[77] only the lower energy absorption edge in the same region was being considered as it was the lowest energy absorption between valence band and conduction band edges. The absorption edge of each plot was extrapolated to the x-axis ($y = 0$). Extrapolated values for $F(\mathrm{R})$ and $F(\mathrm{R})^2$ are 2.03 eV and 2.32 eV respectively. According to the Poeppelmeier method, the optical band gap ($E_g = 2E_2 - E_1$) of $BaBi_2O_6$ was found to be 2.60 eV, which is in good agreement with the calculated direct band gap of 2.90 eV and excellent agreement with the previous experimental report of 2.6 eV.[36]

Dynamical Stability and Lattice Thermal Conductivity

The calculated phonon dispersion of $BaBi_2O_6$ converged against supercell size is displayed in Figure 8. $BaBi_2O_6$ is dynamically stable, with no imaginary modes in the $2 \times 2 \times 2$ or $4 \times 4 \times 4$ supercells used in further calculations. The lattice thermal conductivity of $BaBi_2O_6$ has been converged against q-point mesh and the force constants have been symmetrised, as

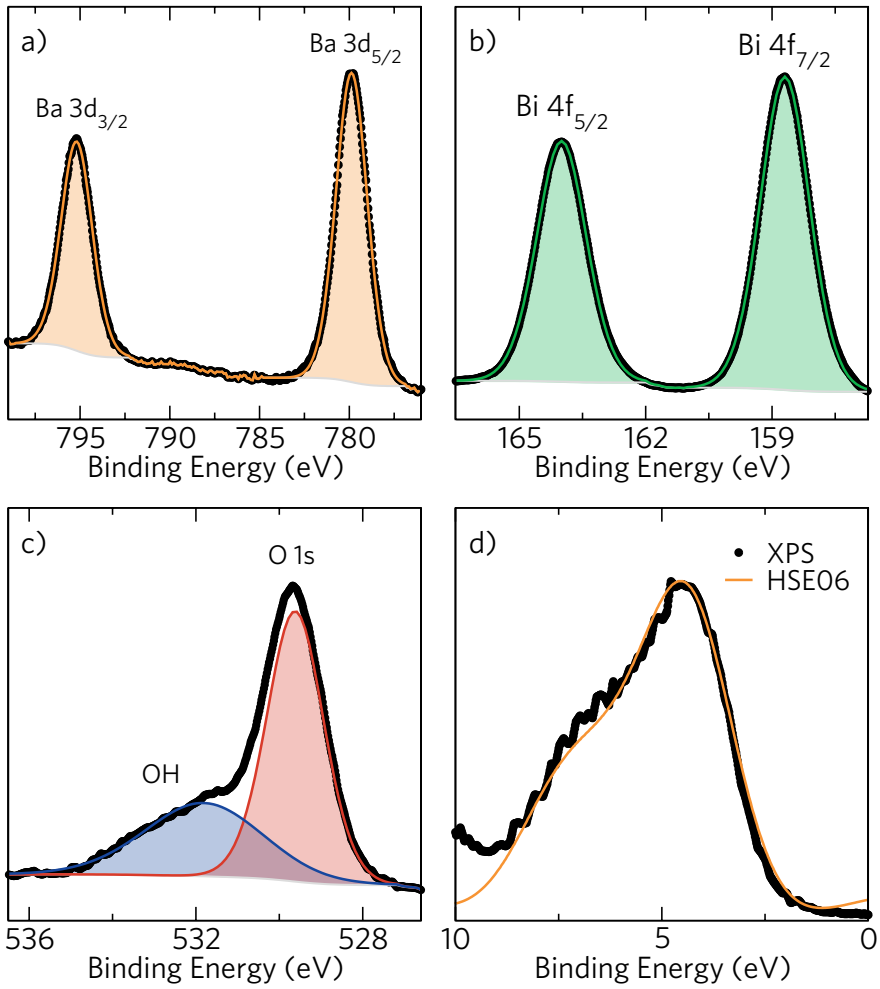

Figure 6: X-ray photoelectron spectra of $BaBi_2O_6$ form experiment (black) and DFT using the HSE06 functional (coloured) using the Galore package.[50] (a) the Ba $3d$ orbitals, (b) the Bi $4f$ orbitals, (c) O-related orbitals and (d) the valence band; all with the Fermi level pinned to 0 eV.

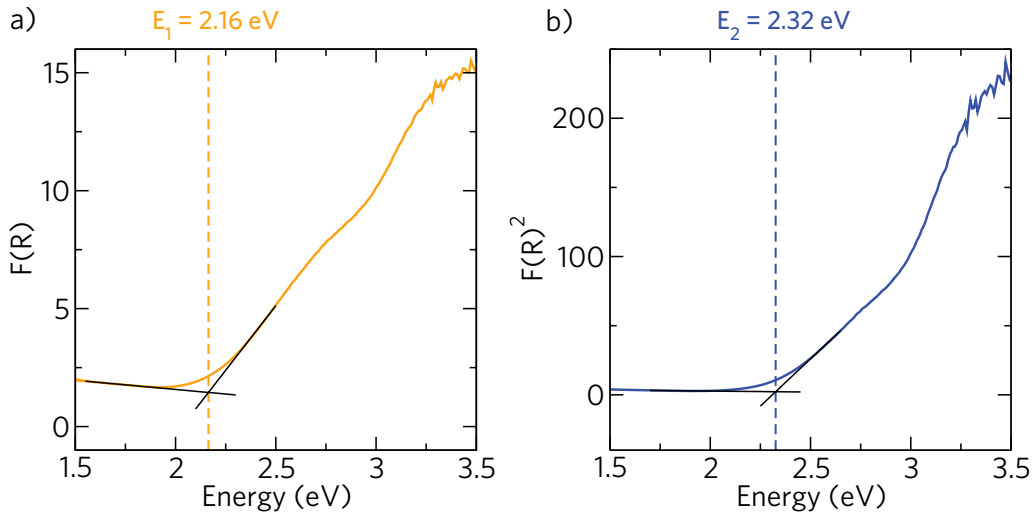

Figure 7: Diffuse reflectance spectra showing Kulbeka–Munk function (a) $F(\mathrm{R})$ and (b) $F(\mathrm{R})^2$.

shown in ESI Figure S2. The lattice thermal conductivity is anisotropic, as is expected from the layered nature of the crystal structure: in the *ab* plane it is $2.08\,\mathrm{W\,m^{-1}\,K^{-1}}$, higher than that along the *c* axis of $1.23\,\mathrm{W\,m^{-1}\,K^{-1}}$ at 600 K. It should be noted that these thermal conductivities are nearly an order of magnitude lower than that reported for some well-known *n*-type oxide thermoelectrics such as ZnO and $SrTiO_3$, with thermal conductivities of $50\,\mathrm{W\,m^{-1}\,K^{-1}}$ [24] and $11\,\mathrm{W\,m^{-1}\,K^{-1}}$ [78] respectively at 300 K, as opposed to $2.4\,\mathrm{W\,m^{-1}\,K^{-1}}$ in the out-of-layer direction here. This is slightly higher than some other low lattice thermal conductivity oxide thermoelectrics, such as Bi_2PdO_4 ($2.2\,\mathrm{W\,m^{-1}\,K^{-1}}$ in the *ab* direction) [79] and $(\mathrm{Na\,Ca})Co_2O_4$ ($1.8\,\mathrm{W\,m^{-1}\,K^{-1}}$). [80]

Defect Chemistry

While the low lattice thermal conductivity and highly dispersive conduction band edge seem to indicate that $BaBi_2O_6$ has the possibility of achieving high ZTs, in practice, it is the defect chemistry of the material which is key. If $BaBi_2O_6$ is not *n*-type dopable, then the high conductivities necessary for high ZT will not be possible. To analyse the defect chemistry of $BaBi_2O_6$ we must first examine the chemical potential stability versus competing phases,

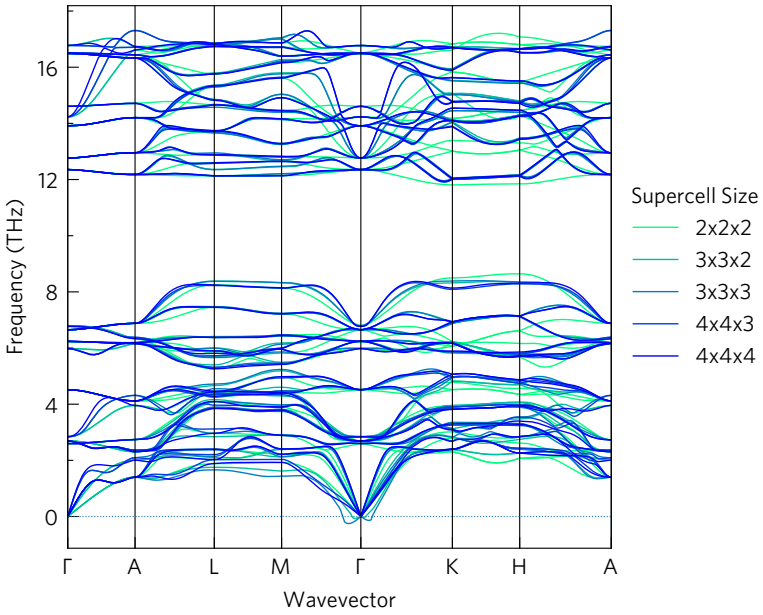

Figure 8: (a) Phonon dispersion of $BaBi_2O_6$ as calculated within the harmonic approximation (PBEsol/DFT) at the equilibrium (athermal) lattice constants using Phonopy[54] and plotted with ThermoPlotter.[81] The k-point path is using the Bradley–Cracknell formalism,[67] and the paths are shown in the Brillouin zone in ESI Figure S3.

in order that we can find the optimum growth conditions to produce n-type $BaBi_2O_6$ (the formation energies of these competing phases as well as $BaBi_2O_6$ itself are listed in ESI Table S1). The HSE06 calculated accessible range of chemical potentials for $BaBi_2O_6$ is illustrated in Figure 9 and tabulated in ESI Table S2, in a two-dimensional (μ_{Ba}, μ_{Bi}) plane, using the CPLAP programme.[82] The vertices of the stability triangle are formed from the host condition ($\mu_{\mathrm{Ba}} + 2\mu_{\mathrm{Bi}} + 6\mu_{\mathrm{O}} \leq \Delta H_{\mathrm{f}}^{\mathrm{BaBi_2O_6}}$), giving the limits of Ba/Bi rich, Ba-poor and Bi-poor environments. Taking into account the constraints imposed by the competing binary oxides and the ternary $Ba_2Bi_2O_5$ phase, the stable range of (μ_{Ba}, μ_{Bi}) for $BaBi_2O_6$ is shaded blue in Figure 9. Within these boundaries, we explicitly considered one environment, as indicated with an orange dot on Figure 9. This environment corresponds to Bi-rich, Ba-rich and O-poor conditions, and is expected to be optimum for n-type defect formation.

Under the different sets of conditions, the solubilities of extrinsic defect-related species are limited by the formation of secondary phases, i.e. $x\mu_{\mathrm{M}} + y\mu_{\mathrm{O}} \leq \Delta H_f^{\mathrm{M}_x\mathrm{O}_y}$. We have

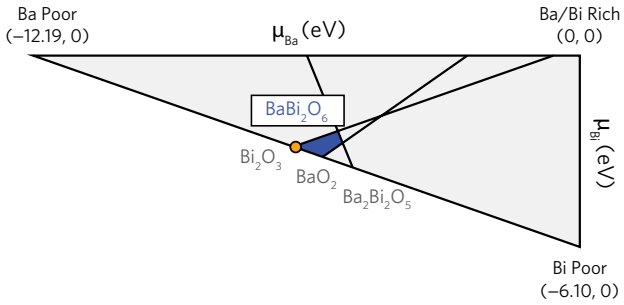

Figure 9: Illustration of the accessible (μ_{Ba}, μ_{Bi}) chemical potential range, calculated with CPLAP.[82] The triangle vertices are determined by the formation enthalpy of $BaBi_2O_6$. Limits imposed by the formation of competing binary and ternary oxides result in the stable region shaded blue. The most n-type growth conditions are indicated with an orange dot. The formation energies of $BaBi_2O_6$ and its competing phases are listed in ESI Table S1, and the chemical potential limits of the stable region of $BaBi_2O_6$ are listed in ESI Table S2.

therefore calculated the formation energy of La_2O_3 using the same calculation parameters as for bulk $BaBi_2O_6$. In the case of F, which substitutes on the O site, the solubility was determined by the formation of $\Delta H_{\mathrm{f}}^{\mathrm{BaF_2}}$.

The native n-type defects considered in this study includes the O vacancy (V_O), Bi on Ba antisite (Bi_{Ba}), Bi and Ba interstitials (Bi_i and Ba_i), while the p-type defects considered were the Ba vacancy (V_{Ba}), Bi vacancy (V_{Bi}), Ba on Bi antisite (Ba_{Bi}), and O interstitial (O_i). As potential n-type dopants, we have selected La as this has been found to be the best dopant for related n-type oxide $BaSnO_3$,[26,83,84] as well as previously untested F doping. F has long been known to be an excellent n-type dopant in SnO_2.[29] La has been considered as a substitutional defect on Bi site (La_{Bi}) and the Ba site (La_{Ba}), while F doping has been considered on the oxygen site (F_O) and as an interstitial (F_i).

A plot of the HSE06 calculated formation energies as a function of Fermi level for all intrinsic defects in $BaBi_2O_6$ under our chosen chemical potential is shown in Figure 10(a). Uniquely, at high Fermi levels (at the CBM), the lowest energy defect is the oxygen interstitial, however it relaxes from the ideal interstitial site towards a lattice oxygen, displacing it to form a peroxide (O–O dumbbell-like) species, which we will now denote as O_{per}, and is shown in ESI Figure S5. The O_{per} does not possess a transition level in the band gap,

indicating that it is electronically inactive in $BaBi_2O_6$ and so will not act as an effective charge compensating defect. This type of behaviour has also been noted previously for other wide band gap n-type oxides.[25,85,86]

V_O is the lowest energy intrinsic donor, however, it is a deep donor, with 2+/1+ and 1+/0 ionisation levels at 0.96 eV and 0.53 eV from the CBM respectively. In most wide band gap n-type oxides, including $BaSnO_3$,[26] Ga_2O_3,[87] In_2O_3,[88–90] SnO_2[88,90–92] and ZnO,[58,88,90,93–100] V_O acts as a negative-U type defect, where only the neutral and the 2+ charge state are stable in the band gap. The presence of all three charge states of V_O in $BaBi_2O_6$ can be rationalised by examining the relaxation around the vacancies in all three charge states. Each oxygen in $BaBi_2O_6$ is coordinated to two Bi ions at a distance of 2.101 Å and to one Ba ion at a distance of 2.747 Å. In the neutral charge state, the Bi ions relax away from the vacancy by 2.2 % of the equilibrium Bi–O bond length, whereas the Ba ion relaxes away from the vacancy site by 6.6 % compared to the equilibrium Ba–O bond length. In the singly ionised (1+) charge state, one of the Bi ions experienced a very strong relaxation away from the vacancy site by 16.2 % compared to the equilibrium bond length, whereas the other Bi ion relaxed away from the vacancy by only 3.7 %. The Ba ion relaxed away by 7.9 %. In the doubly ionised (2+) charge state, the Bi ions relax away from the vacancy by 14.1 %, with the Ba ions relaxing away from the vacancy by 8.4 %. In the case of other wide band gap oxides, the much larger relaxations of the neutral and doubly ionised charge states are the origin of the negative-U defect, whereas for $BaBi_2O_6$, all three states experience quite similar relaxations, and so all three charge states are seen in the band gap.

The Bi_{Ba} antisite is the next most stable defect, and it acts as a one-electron resonant donor in $BaBi_2O_6$. Bi is stabilised as Bi^{3+} on the large Ba site (the ionic radius of 6 coordinate Ba is 1.35 Å, and the ionic radii of 6 coordinate Bi^{3+} and Bi^{5+} are 1.03 Å and 0.76 Å respectively). Bi_i and Ba_i both act as shallow donors, but are considerably higher in energy and are unlikely to play a large role in conductivity in $BaBi_2O_6$. The lowest energy native acceptor defect is the V_{Ba}, but it is too high in energy to compensate the V_O and

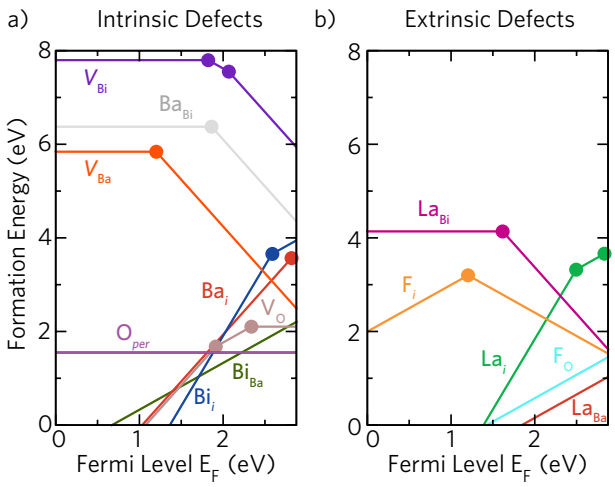

Figure 10: Formation energies for (a) intrinsic defects and (b) extrinsic defects in $BaBi_2O_6$ under the condition chosen in Figure 9. The slope of the lines denotes the charge state; the larger the slope, the bigger the charge state. The solid dots represent the transition levels $\epsilon(D, q/q')$.

the Bi_{Ba} until the Fermi level is above the CBM. All p-type defects are ultra deep in nature, which is to be expected for a material with an O $2p$ dominated valence band.[26,28,92] Taken together, this native defect equilibria indicates that $BaBi_2O_6$ is a weakly n-type material, which will not have a large amount of charge carriers due to the high formation energies of donors when the Fermi level is at the CBM (all defects above 2.0 eV). It is clear that to realise high conductivities in $BaBi_2O_6$ that an efficient extrinsic dopant is necessary.

In Figure 10(b) we present a plot of formation energy as a function of Fermi level for our chosen extrinsic defects in $BaBi_2O_6$. La_{Ba} and F_O are both resonant donors in this system, with La_{Ba} the most soluble defect with formation energy of 1.0 eV at the CBM. La_{Bi} has a formation energy of 4.14 eV, and is a deep acceptor, but will not compensate La_{Ba} under these growth conditions until the Fermi energy is above the CBM. F_i is an amphoteric defect, but is too high in energy to compensate the low energy F_O, which indicates that F doping is another viable alternative dopant to La for producing a degenerate n-type $BaBi_2O_6$.

To confirm these results, we used the SC-Fermi code[65] to determine the achievable carrier concentrations. Under equilibrium conditions at 300 K, we found $BaBi_2O_6$ to be essentially undoped intrinsically, with its Fermi level at 1.86 eV above the VBM. Introducing a La

dopant, still under equilibrium conditions, sets the concentration to 4.7×10^{11} electrons cm^{-3} via singly charged $\mathrm{La_{Ba}}$ cations, but only raises the Fermi level to 2.4 eV above the VBM, 0.5eV below the CBM. F introduced 3.4×10^{8} electrons cm^{-3} via singly charged $\mathrm{F_O}$ cations, raising the Fermi level to 2.3 eV above the VBM. In order to investigate realistic conditions, where dopants may be introduced at non-equilibrium concentrations, the main extrinsic defects ($\mathrm{La_{Ba}}$ or $\mathrm{F_O}$) were fixed at various concentrations to see the response of other defects, and therefore what doping concentrations may be reached. In both cases, concentrations of the order of 1×10^{20} electrons cm^{-3}, or about 3 eV above the VBM, are achievable, around which point the majority of new dopant atoms form neutral defects, and the electron concentration ceases to rise very fast. As predicted, La is the more effective dopant, as with 1×10^{20} dopants cm^{-3}, 7×10^{19} electrons cm^{-3} are generated, whereas for F, only 2×10^{19} electrons cm^{-3} are (see also ESI Figure S4). From these results, it is clear that La is the ideal dopant for $\mathrm{BaBi_2O_6}$, as it the most soluble, it will not be compensated until well above the CBM, allowing high carrier concentrations to be reached, and the mass difference between La and Ba on the Ba lattice site should suppress the lattice thermal conductivity.

Electronic Transport Properties

Our results thus far have demonstrated that $\mathrm{BaBi_2O_6}$ possesses a low lattice thermal conductivity, and the correct defect chemistry when donor doped with La to modulate the Fermi energy into the conduction band. Now we use Boltzmann transport theory within the AMSET code[52] to calculate the electronic conductivity, Seebeck coefficient and electronic contribution to the thermal conductivity in order to calculate ZT. We have also used the BoltzTraP code,[51] which will be discussed in the next section.

In Figure 11 we demonstrate colour maps of achievable ZTs versus carrier concentration and temperature in the in-layer (ab) and out-of-layer (c) directions. We can see that at high temperatures of $\sim$600 K, the maximum ZT occurs at a carrier concentration of 6.3×10^{19} carriers cm^{-3}. From our SC-Fermi analysis, this is equivalent to a La

dopant concentration of 9×10^{19} dopants cm^{-3} (or 0.3 % w/w), or a F concentration of 3×10^{21} dopants cm^{-3} (or 1.4 % w/w). At these concentrations, a ZT of 0.18 is achievable in the in-layer direction, and 0.19 can be reached in the out-of-layer direction. While smaller than the ZT achieved by the archetypal n-type earth-abundant thermoelectric $SrTiO_3$ at 570 K of 0.22,[101] in a real (imperfect crystal) device, the lattice thermal conductivity would be expected to be lower, and further research into $BaBi_2O_6$ may also enhance these values.

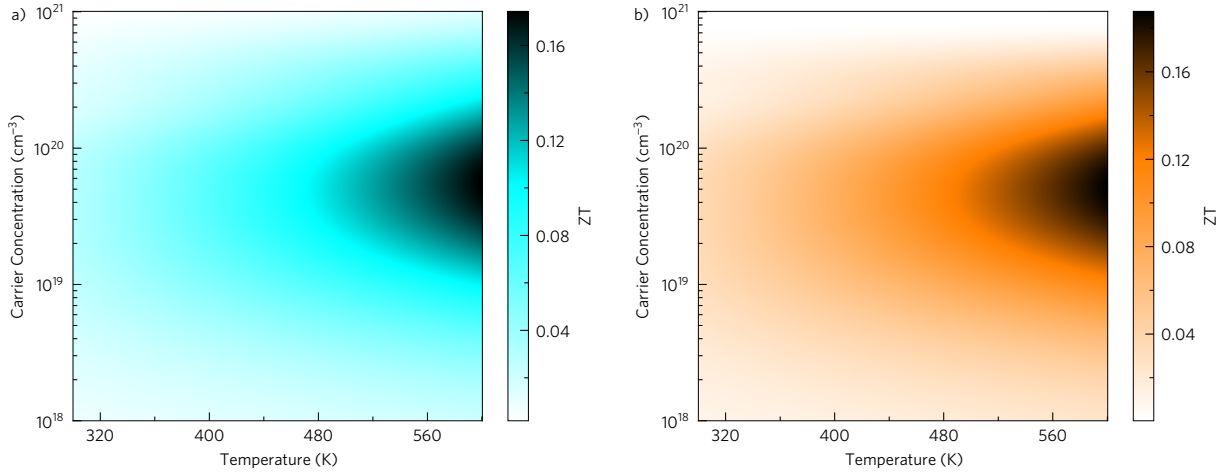

Figure 11: ZT of single-crystal $BaBi_2O_6$ against temperature and carrier concentration in the (a) in-layer (ab) and (b) out-of-layer (c) directions. The darkest colours indicate the highest ZT. This and all subsequent figures utilise ThermoPlotter.[81]

Discussion

To computationally predict the potential of a material as a thermoelectric, we must ensure: (i) that our description of the electronic structure is of a high quality, (ii) that we can computationally predict the lattice thermal conductivity, and (iii) that we have a proper understanding of the defect chemistry. For $BaBi_2O_6$, we have used hybrid DFT for the description of the electronic structure, a high level of theory known to find accurate electronic properties, from which we demonstrate low electron effective masses. This indicates good electrical conductivity when n-type doped, which we then showed to be possible with La and F. We then used the AMSET and BoltzTraP codes to determine the electronic transport

properties. BoltzTraP was released in 2006 and is widely used due to its computational cheapness, due to its use of a constant relaxation time, in this work set to $1 \times 10^{-14}\,\mathrm{s}^{-1}$. As computational techniques and resources advance, it has become possible to go beyond a constant lifetime. Here we calculated the deformation potentials, elastic constants, and static and high-frequency dielectric constants of $BaBi_2O_6$ in order to calculate the acoustic deformation potential (ADP), ionised-impurity (IMP) and polar optical phonon (POP) scattering using AMSET (more details can be found in the ESI). Figure 12 shows the electronic transport properties calculated from AMSET and BoltzTraP, which we can see broadly agree at low temperatures and carrier concentrations, but the electrical and electronic thermal conductivities diverge between the codes as the temperature and carrier concentration decrease.

To investigate, we compared the temperature and carrier concentration dependence of the scattering rates (Figure 13). We plotted the average transport rate, defined as $\tau_\mathrm{t}^{-1} = \int \tau^{-1}(-\,\mathrm{d}f/\mathrm{d}\varepsilon)\,\mathrm{d}\varepsilon \,/\, \int(-\,\mathrm{d}f/\mathrm{d}\varepsilon)\,\mathrm{d}\varepsilon$ in which the rates (τ^{-1}) are weighted by the derivative of the Fermi–Dirac distribution ($\mathrm{d}f/\mathrm{d}\varepsilon$) at each temperature and doping concentration, as they are in the Boltzmann transport equation. This metric provides a better reflection of how the scattering rates that actually contribute to transport change at different conditions. IMP scattering does not vary strongly with temperature, and while ADP scattering increases with temperature, its rate of scattering is too low to have much effect on the overall rate, which means the increase in scattering and consequent decrease in conductivity with temperature is driven by POP scattering. POP scattering also drives the trend against carrier concentration at low temperatures, where the increased screening from the extra electrons reduces the rate of scattering. In contrast, IMP scattering naturally rapidly increases with increased carrier concentration, as it is due to a greater number of ionised impurities, and at carrier concentrations over $4 \times 10^{19}\,\mathrm{carriers\,cm}^{-3}$, it becomes the dominant scattering mechanism. Together, these effects result in a minimum total scattering rate at 600 K of between 1×10^{19}–$1 \times 10^{20}\,\mathrm{carriers\,cm}^{-3}$, which is where the maximum ZT occurs. This behaviour also predicts

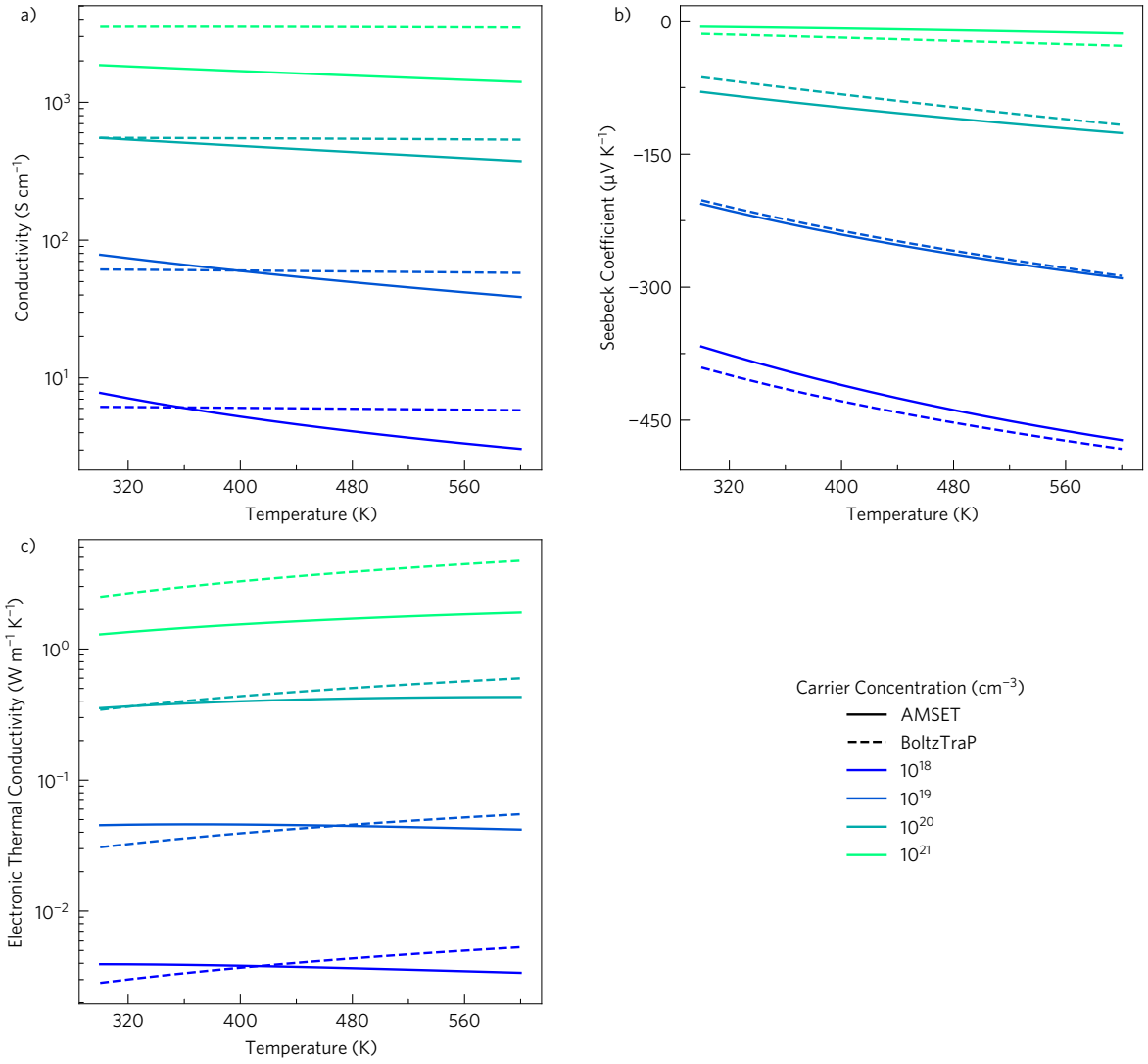

Figure 12: Direction-averaged (a) electrical conductivity, (b) Seebeck coefficient and (c) electronic thermal conductivity of $BaBi_2O_6$ against temperature for several carrier concentrations from AMSET and BoltzTraP.

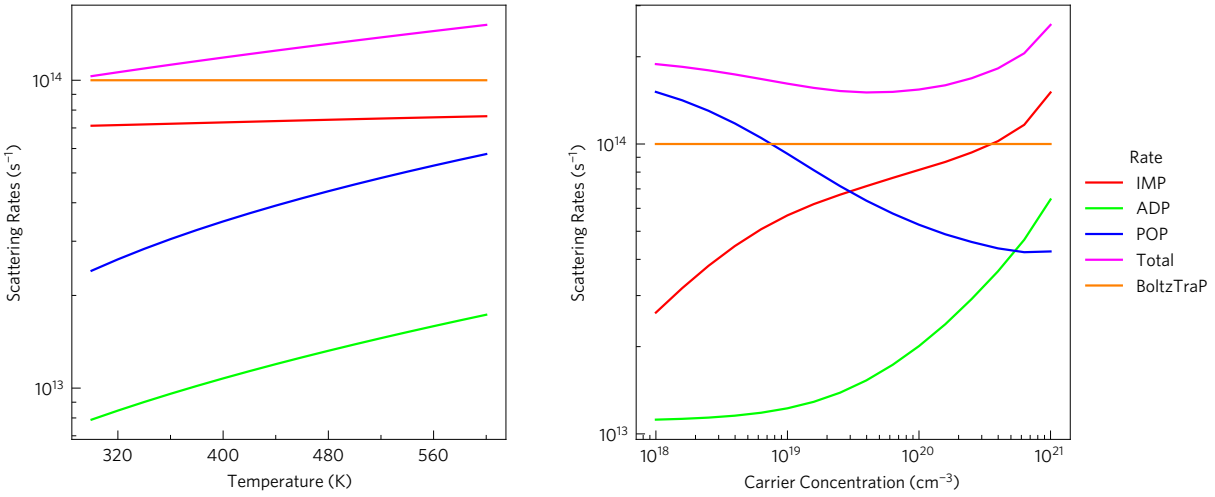

Figure 13: The rates are averaged over k-points and weighted by the normalised energy derivative of the Fermi–Dirac distribution. IMP is ionised impurity scattering (red), ADP is acoustic deformation potential scattering (green) and POP is polar optical phonon scattering (blue), which are summed to get total (pink). The constant relaxation time (CRT) used by BoltzTraP is also shown (orange).

the trend in the optimal carrier concentration to minimise the scattering with temperature: as temperature decreases, the rate of POP scattering decreases, shifting the intercept of the two rates to lower carrier concentrations. Note, however, this does not predict the optimal carrier concentration for conductivity, which increases with more carriers; or that for ZT, which does decrease with temperature, but not to the extent that the scattering rate does. Due to its lesser dependence on scattering, the Seebeck coefficient agrees relatively well between the two codes, so overall the lower scattering in BoltzTraP leads to an inflated power factor, as well as a reduced optimal carrier concentration.

Using these AMSET results at 300 K and 1×10^{20} carriers cm^{-3}, around the maximum carrier concentration reasonably reachable, we predict direction-averaged conductivities of 5.5×10^3 S cm^{-1}, and in the in-layer direction, the conductivity reaches 6.2×10^3 S cm^{-1}, equating to an electron mobility of 38.8 cm^2 V^{-1} s^{-1}, or 34.4 cm^2 V^{-1} s^{-1} if directionally averaged (see also ESI Figure S6). These are large values, and raise the possibility of an alternative application for $BaBi_2O_6$ as an electron transport layer. Together with a moderate Seebeck coefficient, such conductivities give a power factor in the in-layer direction at

600 K of 7.00×10^{-4} W m^{-1} K^{-2} with 6.3×10^{19} carriers cm^{-3}, while the out-of-layer direction only reaches 4.44×10^{-4} W m^{-1} K^{-2}. These are lower than those reported for $SrTiO_3$ (8×10^{-4}–1.3×10^{-3} W m^{-1} K^{-2}),[18,102–105] indicating that the key factor in achieving these ZTs comes from the low lattice thermal conductivity.

It must be noted that our computational prediction is based on the electronic structure and thermal conductivity of a perfect crystal, but in a real material imperfections in the crystal will reduce the lattice thermal conductivity. From Figure 14(a), we can see that the

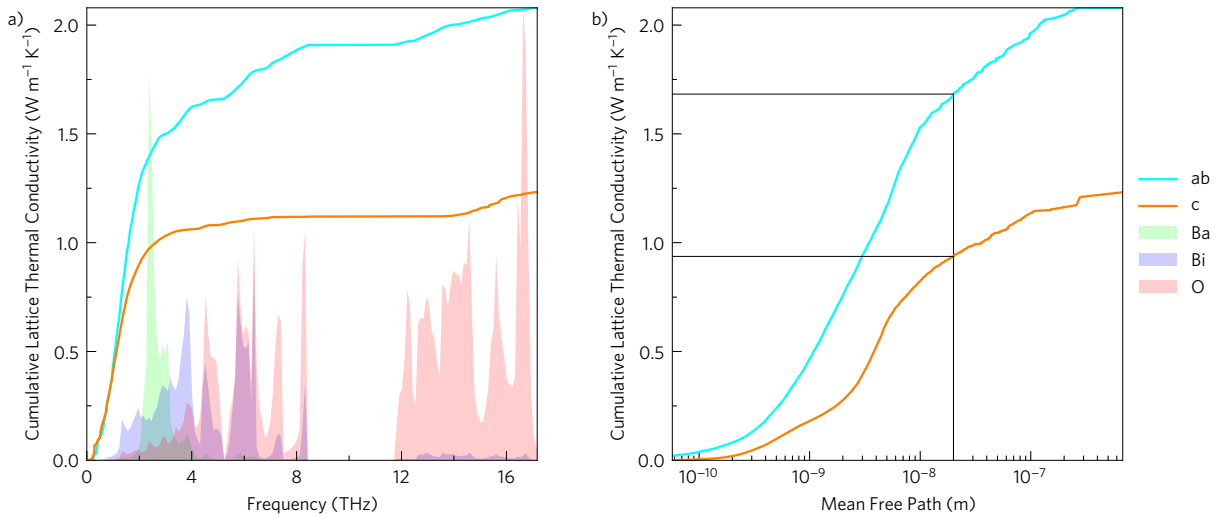

Figure 14: The direction-averaged cumulative lattice thermal conductivity at 600 K of $BaBi_2O_6$ against (a) frequency, with the phonon density of states overlaid and (b) mean free path, with markers showing the lattice thermal conductivity of the phonons of mean free path less than 20 nm.

phonon modes below 4 THz cause 75 % of the lattice thermal conductivity, and that these modes are dominated by the Ba and Bi atoms. As the proposed La dopant would occupy a Ba site, this may produce a greater reduction in the lattice thermal conductivity compared to, for example, a F dopant, as the O sites which the F dopant would occupy have comparatively little effect on the lattice thermal conductivity. In addition, experimental samples are typically pressed and sintered pellets, so the lattice thermal conductivity is generally lower due to the presence of grain boundaries. Beyond this, there is a strong research drive to find mechanisms to reduce the lattice thermal conductivity of potential thermoelectric

materials, such as by introducing more grain boundaries to intentionally minimise the lattice thermal conductivity in a process called nanostructuring. The thermoelectric PbTe has been nanostructured as $AgPb_{18}SbTe_{20}$ to a grain size of around 20 nm,[5] which enhanced its ZT from $\sim$0.5[106] to 2.2. Figure 14(b) shows the cumulative lattice thermal conductivity against mean free path of $BaBi_2O_6$. $BaBi_2O_6$ has a similar mean free path distribution compared to PbTe, with 20–25 % of the lattice thermal conductivity coming from modes with a mean free path larger than 20 nm at 600 K,[107] so nanostructuring may have a large effect on the lattice thermal conductivity and should increase ZT. To estimate what effect a similar level of nanostructuring would have on $BaBi_2O_6$, the mean free paths of the phonons were capped to 20 nm in Phono3py to recalculate the lattice thermal conductivity. Such nanostructuring will also contribute to electron scattering. Accordingly, we have included the same restriction on the mean free path of electrons in AMSET, ensuring a complete description of the effects of grain size on electronic and vibrational properties. Figure 15 shows the conductivity (σ), Seebeck coefficient (α), power factor ($\alpha^2\sigma$) and lattice thermal conductivity at 600 K and 6.3×10^{19} carriers cm^{-3} for the ab and c directions, as well as the averaged direction for a polycrystalline sample where the charge carrier and phonon mean free paths are not limited, and the same where they are limited to 20 nm. The Seebeck coefficient does not vary much between the directions or crystal sizes, but in the c direction the electrical conductivity decreases by a third relative to the ab direction. This causes a decrease in the power factor, but due to the reduced lattice thermal conductivity, overall there is still an increase in ZT. Nanostructuring, on the other hand, only reduces the electrical conductivity by about 15 % relative to an averaged, but not nanostructured sample, but the lattice thermal conductivity is reduced below that of the c direction, particularly at lower temperatures where thermal vibrations cause less scattering. This causes the ZT of nanostructured $BaBi_2O_6$ to be slightly higher than a single crystal in the c direction, at 0.22 at 600 K and 6.3×10^{19} carriers cm^{-3}. The non-nanostructured, still polycrystalline version has a ZT of 0.18 under the same conditions. As shown in Table 4, BoltzTraP does not

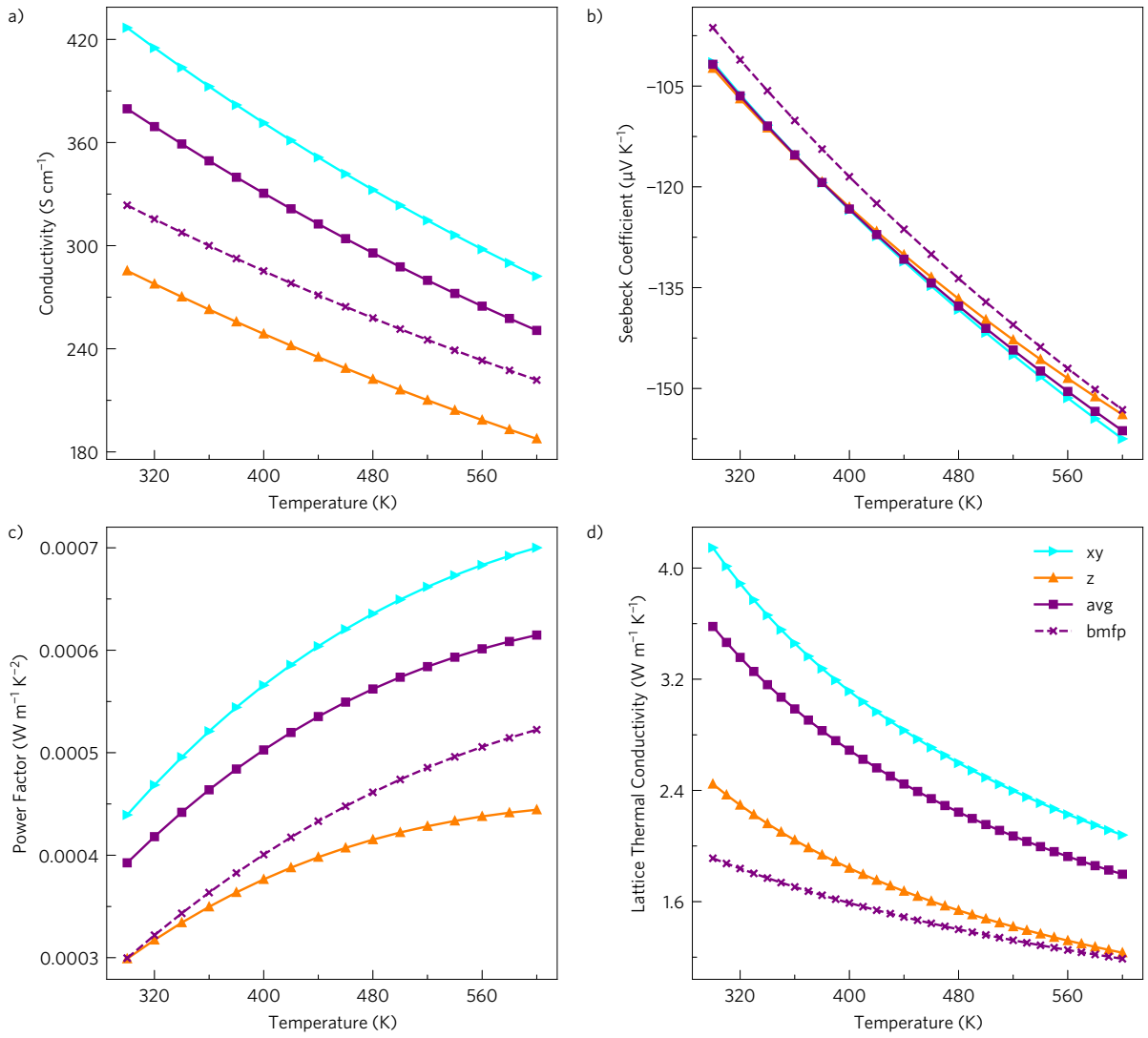

Figure 15: (a) Electrical conductivity, (b) Seebeck coefficient, (c) power factor and (d) lattice thermal conductivity of $BaBi_2O_6$ against temperature at 6.3×10^{19} carriers cm^{-3} in the in-layer (ab), out-of-layer (c) directions, the averaged value (avg) and the averaged value with a maximum mean free path (bmfp) of 20 nm.

take into account these nuances, so the conductivities, which are already larger than those for AMSET at this temperature and carrier concentration, are not reduced, leading to an inflated ZT prediction of 0.3.

Table 4: ZT from BoltzTraP and AMSET in the in-layer (ab), out-of-layer (c) and average directions, the latter additionally with a boundary mean free path of 20 nm applied, along with the carrier concentration (n) and power factor (PF) at that point at 600 K.

Direction	BoltzTraP			AMSET		
	n (cm^{-3})	PF ($\mathrm{W\,m^{-1}\,K^{-2}}$)	ZT	n (cm^{-3})	PF ($\mathrm{W\,m^{-1}\,K^{-2}}$)	ZT
ab	4.0×10^{19}	8.38×10^{-4}	0.21	6.3×10^{19}	7.00×10^{-4}	0.17
c	4.0×10^{19}	4.82×10^{-4}	0.21	6.3×10^{19}	4.44×10^{-4}	0.19
avg	4.0×10^{19}	7.20×10^{-4}	0.21	6.3×10^{19}	6.15×10^{-4}	0.18
bmfp	4.0×10^{19}	7.20×10^{-4}	0.30	6.3×10^{19}	5.22×10^{-4}	0.22

Overall, these factors make $BaBi_2O_6$ a remarkably versatile thermoelectric: The polycrystalline, but not nanostructured material, the easiest to make of the options, has a ZT of 0.18, which while lower that the leading low-temperature, earth abundant thermoelectric, $SrTiO_3$, has not had nearly the amount of research dedicated to it. If instead it were grown single-crystal, a modest increase in ZT could be achieved, reaching 0.19; or if instead $BaBi_2O_6$ could be nanostructured to around 20 nm, the ZT could be increased to 0.22, the same as $SrTiO_3$. Again, with more research, these vales could likely be exceeded. It is also worth noting the high conductivity of $6.2 \times 10^3\,\mathrm{S\,cm^{-1}}$ in the ab direction with $1 \times 10^{20}\,\mathrm{carriers\,cm^{-3}}$ at 300 K, suggesting $BaBi_2O_6$ could be an effective electron transport layer.

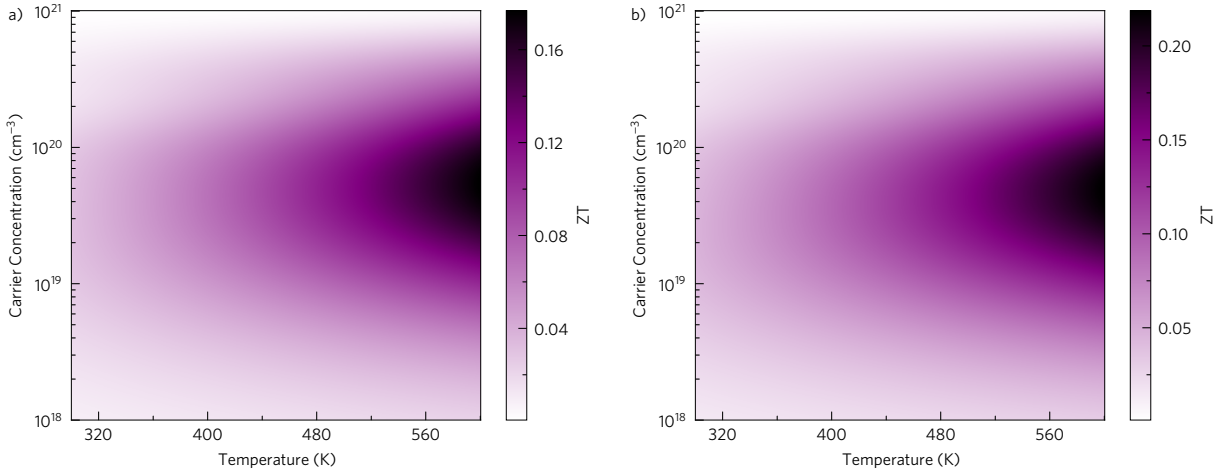

Figure 16: (a) Direction-averaged ZT of $BaBi_2O_6$ against temperature and carrier concentration, simulating a powdered, but not nanostructured sample. (b) The same, but with mean free paths of phonons and electrons limited to 20 nm, simulating a nanostructured sample. The darkest colours indicate the highest ZT.

Conclusions

We have prepared the earth-abundant $PbSb_2O_6$-structured material $BaBi_2O_6$ via a solution-processable method under benign conditions. We then used state-of-the-art *ab-initio* calculations to screen it for thermoelectric properties. We have demonstrated that $BaBi_2O_6$ possesses the ideal electronic structure for high n-type conductivity, with electron mobilities of 30–40 $cm^2\,V^{-1}\,s^{-1}$ at 300 K with 1×10^{20} carriers cm^{-3}, which means it could be suitable as an electric transport layer. $BaBi_2O_6$ also displays a moderate Seebeck coefficient and a much lower lattice thermal conductivity than other n-type thermoelectric oxides, and can be La-doped to become a degenerate semiconductor. We have computationally predicted a powdered (that is, directionally averaged) ZT of 0.18 at 600 K which could be competitive with the much more heavily studied $SrTiO_3$ at a similar temperature. Our analysis indicates that single-crystal $BaBi_2O_6$ could give an enhanced ZT of 0.19 in the out-of-layer direction due to its suppressed lattice thermal conductivity, or alternatively nanostructuring will be an effective mechanism to lower the lattice thermal conductivity even further, without such a large decrease in electrical conductivity, leading to a ZT of 0.22. We further showed

the importance of fully simulating the scattering process in potential thermoelectrics, to avoid overestimating the potential ZT. Together, these results demonstrate $BaBi_2O_6$ to be promising, sustainable thermoelectric material with the potential to surpass $SrTiO_3$. We also expect that the $PbSb_2O_6$ structure type will be a fruitful structural motif in the search for novel oxide thermoelectrics.

Acknowledgements

Via our membership of the UK's HEC Materials Chemistry Consortium, which is funded by EPSRC (EP/L000202, EP/R029431, EP/T022213), this work used the ARCHER UK National Supercomputing Service (http://www.archer.ac.uk); and the UK Materials and Molecular Modelling Hub for computational resources, MMM Hub, which is also partially funded by EPSRC (EP/P020194 and EP/T022213). This work used the ARCHER2 UK National Supercomputing Service (https://www.archer2.ac.uk). The authors acknowledge the use of the UCL Legion, Myriad, Grace and Kathleen High Throughput Computing Facilities (Legion@UCL, Myriad@UCL, Grace@UCL and Kathleen@UCL), and associated support services, in the completion of this work. DOS acknowledges support from the EPSRC (EP/N01572X/1). DOS acknowledges membership of the Materials Design Network. AMG acknowledges Diamond Light Source for the co-sponsorship of a studentship on the EPSRC Centre for Doctoral Training in Molecular Modelling and Materials Science (EP/L015862/1).

Conflict of Interest

The authors declare no competing financial interest.

References

(1) Peters, G. P.; Andrew, R. M.; Boden, T.; Canadell, J. G.; Ciais, P.; Le Quéré, C.; Marland, G.; Raupach, M. R.; Wilson, C. The Challenge to Keep Global Warming Below 2°C. *Nat. Clim. Change* **2012**, *3*, 4.

(2) Firth, A.; Zhang, B.; Yang, A. Quantification of Global Waste Heat and its Environmental Effects. *Appl. Energy* **2019**, *235*, 1314.

(3) Franz, R.; Wiedemann, G. Über die Wärme-Leitungsfähigkeit der Metalle. *Ann. Phys.* **1853**, *165*, 497.

(4) Slack, G. A. In *CRC Handbook of Thermoelectrics*, 1st ed.; Rowe, D. M., Ed.; CRC Press: Boca Raton, 1995; Chapter 34, pp 407–440.

(5) Hsu, K. F.; Loo, S.; Guo, F.; Chen, W.; Dyck, J. S.; Uher, C.; Hogan, T.; Polychroniadis, E. K.; Kanatzidis, M. G. Cubic $AgPb_mSbTe_{2+m}$: Bulk Thermoelectric Materials with High Figure of Merit. *Science* **2004**, *303*, 818.

(6) Biswas, K.; He, J.; Blum, I. D.; Wu, C.-I.; Hogan, T. P.; Seidman, D. N.; Dravid, V. P.; Kanatzidis, M. G. High-Performance Bulk Thermoelectrics with All-Scale Hierarchical Architectures. *Nature* **2012**, *489*, 414.

(7) Korkosz, R. J.; Chasapis, T. C.; Lo, S.-h.; Doak, J. W.; Kim, Y. J.; Wu, C.-I.; Hatzikraniotis, E.; Hogan, T. P.; Seidman, D. N.; Wolverton, C.; Dravid, V. P.; Kanatzidis, M. G. High ZT in *p*-Type $(PbTe)_{1-2x}(PbSe)_x(PbS)_x$ Thermoelectric Materials. *J. Am. Chem. Soc.* **2014**, *136*, 3225.

(8) Wu, H. J.; Zhao, L.-D.; Zheng, F. S.; Wu, D.; Pei, Y. L.; Tong, X.; Kanatzidis, M. G.; He, J. Q. Broad Temperature Plateau for Thermoelectric Figure of Merit ZT > 2 in Phase-Separated $PbTe_{0.7}S_{0.3}$. *Nat. Commun.* **2014**, *5*, 4515.

(9) Fu, T.; Yue, X.; Wu, H.; Fu, C.; Zhu, T.; Liu, X.; Hu, L.; Ying, P.; He, J.; Zhao, X. Enhanced Thermoelectric Performance of PbTe Bulk Materials with Figure of Merit zT > 2 by Multi-Functional Alloying. *J. Materiomics* **2016**, *2*, 141.

(10) Venkatasubramanian, R.; Colpitts, T.; Watko, E.; Lamvik, M.; El-Masry, N. MOCVD of Bi_2Te_3, Sb_2Te_3 and their Superlattice Structures for Thin-Film Thermoelectric Applications. *J. Cryst. Growth* **1997**, *170*, 817.

(11) Zhao, L.-D.; Lo, S.-H.; Zhang, Y.; Sun, H.; Tan, G.; Uher, C.; Wolverton, C.; Dravid, V. P.; Kanatzidis, M. G. Ultralow Thermal Conductivity and High Thermoelectric Figure of Merit in SnSe Crystals. *Nature* **2014**, *508*, 373.

(12) Terasaki, I.; Sasago, Y.; Uchinokura, K. Large Thermoelectric Power in $NaCo_2O_4$ Single Crystals. *Phys. Rev. B* **1997**, *56*, R12685.

(13) Fujita, K.; Mochida, T.; Nakamura, K. High-Temperature Thermoelectric Properties of $Na_xCoO_{2-\delta}$ Single Crystals. *Jpn. J. Appl. Phys.* **2001**, *40*, 4644.

(14) Funahashi, R.; Shikano, M. $Bi_2Sr_2Co_2O_y$ Whiskers with High Thermoelectric Figure of Merit. *Appl. Phys. Lett.* **2002**, *81*, 1459.

(15) Einhorn, M.; Williamson, B. A. D.; Scanlon, D. O. Computational Prediction of the Thermoelectric Performance of LaZnOPn (Pn = P, As). *J. Mater. Chem. A* **2020**, *8*, 7914.

(16) Koumoto, K.; Terasaki, I.; Funahashi, R. Complex Oxide Materials for Potential Thermoelectric Applications. *MRS Bull.* **2006**, *31*, 206.

(17) Wang, Y.; Sui, Y.; Fan, H.; Wang, X.; Su, Y.; Su, W.; Liu, X. High Temperature Thermoelectric Response of Electron-Doped $CaMnO_3$. *Chem. Mater.* **2009**, *21*, 4653.

(18) Ohta, H.; Sugiura, K.; Koumoto, K. Recent Progress in Oxide Thermoelectric Materials: *p*-Type $Ca_3Co_4O_9$ and *n*-Type $SrTiO_3$. *Inorg. Chem.* **2008**, *47*, 8429.

(19) Molinari, M.; Tompsett, D. A.; Parker, S. C.; Azough, F.; Freer, R. Structural, Electronic and Thermoelectric Behaviour of $CaMnO_3$ and $CaMnO_{3-\delta}$. *J. Mater. Chem. A* **2014**, *2*, 14109.

(20) Daniels, L. M.; Savvin, S. N.; Pitcher, M. J.; Dyer, M. S.; Claridge, J. B.; Ling, S.; Slater, B.; Cora, F.; Alaria, J.; Rosseinsky, M. J. Phonon-Glass Electron-Crystal Behaviour by A Site Disorder in *n*-Type Thermoelectric Oxides. *Energy Environ. Sci.* **2017**, *10*, 1917.

(21) Tsubota, T.; Ohtaki, M.; Eguchi, K.; Arai, H. Thermoelectric Properties of Al-Doped ZnO as a Promising Oxide Material for High-Temperature Thermoelectric Conversion. *J. Mater. Chem.* **1997**, *7*, 85.

(22) Bérardan, D.; Guilmeau, E.; Maignan, A.; Raveau, B. In_2O_3: Ge, a Promising *n*-Type Thermoelectric Oxide Composite. *Solid State Commun.* **2008**, *146*, 97.

(23) Ohtaki, M.; Araki, K.; Yamamoto, K. High Thermoelectric Performance of Dually Doped ZnO Ceramics. *J. Electron. Mater.* **2009**, *38*, 1234.

(24) Spooner, K. B.; Ganose, A. G.; Scanlon, D. O. Assessing the Limitations of Transparent Conducting Oxides as Thermoelectrics. *J. Mater. Chem. A* **2020**,

(25) Burbano, M.; Scanlon, D. O.; Watson, G. W. Sources of Conductivity and Doping Limits in CdO from Hybrid Density Functional Theory. *J. Am. Chem. Soc* **2011**, *133*, 15065.

(26) Scanlon, D. O. Defect Engineering of $BaSnO_3$ for High-Performance Transparent Conducting Oxide Applications. *Phys. Rev. B* **2013**, *87*, 161201.

(27) Scanlon, D. O.; Regoutz, A.; Egdell, R. G.; Morgan, D. J.; Watson, G. W. Band Gap Engineering of In_2O_3 by Alloying with Tl_2O_3. *Appl. Phys. Lett.* **2013**, *103*, 262108.

(28) Dixon, S. C.; Sathasivam, S.; Williamson, B. A. D.; Scanlon, D. O.; Carmalt, C. J.; Parkin, I. P. Transparent Conducting n-Type ZnO:Sc — Synthesis, Optoelectronic Properties and Theoretical Insight. *J. Mater. Chem. C* **2017**, *5*, 7585.

(29) Swallow, J. E. N.; Williamson, B. A. D.; Whittles, T. J.; Birkett, M.; Featherstone, T. J.; Peng, N.; Abbott, A.; Farnworth, M.; Cheetham, K. J.; Warren, P.; Scanlon, D. O.; Dhanak, V. R.; Veal, T. D. Self-Compensation in Transparent Conducting F-Doped SnO_2. *Adv. Funct. Mater.* **2018**, *28*, 1701900.

(30) Powell, M. J.; Williamson, B. A. D.; Baek, S.-Y.; Manzi, J.; Potter, D. B.; Scanlon, D. O.; Carmalt, C. J. Phosphorus Doped SnO_2 Thin Films for Transparent Conducting Oxide Applications: Synthesis, Optoelectronic Properties and Computational Models. *Chem. Sci.* **2018**, *9*, 7968.

(31) Swallow, J. E. et al. Resonant Doping for High Mobility Transparent Conductors: the Case of Mo-Doped In_2O_3. *Mater. Horiz.* **2019**,

(32) Gorai, P.; Stevanović, V.; Toberer, E. S. Computationally Guided Discovery of Thermoelectric Materials. *Nat. Rev. Mater.* **2017**, *2*, 17053.

(33) Funahashi, R.; Matsubara, I.; Sodeoka, S. Thermoelectric Properties of $Bi_2Sr_2Co_2O_x$ Polycrystalline Materials. *Appl. Phys. Lett.* **2000**, *76*, 2385.

(34) Zhao, L. D.; Berardan, D.; Pei, Y. L.; Byl, C.; Pinsard-Gaudart, L.; Dragoe, N. $Bi_{1-x}Sr_xCuSeO$ Oxyselenides as Promising Thermoelectric Materials. *Appl. Phys. Lett.* **2010**, *97*, 092118.

(35) Rahim, W.; Skelton, J. M.; Scanlon, D. O. α-$Bi_2Sn_2O_7$: a Potential Room Temperature n-Type Oxide Thermoelectric. *J. Mater. Chem. A* **2020**, *8*, 16405.

(36) Mizoguchi, H.; Woodward, P. M. Electronic Structure Studies of Main Group Ox-

ides Possessing Edge-Sharing Octahedra: Implications for the Design of Transparent Conducting Oxides. *Chem. Mater.* **2004**, *16*, 5233.

(37) Basso, R.; Lucchetti, G.; Zefiro, L.; Palenzona, A. Rosiaite, $PbSb_2O_6$, a New Mineral from the Cetine Mine, Siena, Italy. *Eur. J. Mineral.* **1996**, *8*, 487.

(38) Momma, K.; Izumi, F. VESTA 3 for Three-Dimensional Visualization of Crystal, Volumetric and Morphology Data. *J. Appl. Crystallogr.* **2011**, *44*, 1272.

(39) Saiduzzaman, M.; Yanagida, S.; Takei, T.; Moriyoshi, C.; Kuroiwa, Y.; Kumada, N. Hydrothermal Synthesis, Crystal Structure, and Visible-Region Photocatalytic Activity of $BaBi_2O_6$. *ChemistrySelect* **2017**, *2*, 4843.

(40) Kresse, G.; Hafner, J. *Ab Initio* Molecular Dynamics for Liquid Metals. *Phys. Rev. B* **1993**, *47*, 558.

(41) Kresse, G.; Hafner, J. *Ab Initio* Molecular-Dynamics Simulation of the Liquid-Metal Amorphous–Semiconductor Transition in Germanium. *Phys. Rev. B* **1994**, *49*, 14251.

(42) Kresse, G.; Furthmüller, J. Efficient Iterative Schemes for *ab Initio* Total-Energy Calculations Using a Plane-Wave Basis Set. *Phys. Rev. B* **1996**, *54*, 11169.

(43) Kresse, G.; Furthmüller, J. Efficiency of *ab Initio* Total Energy Calculations for Metals and Semiconductors Using a Plane Wave Basis Set. *Comput. Mater. Sci.* **1996**, *6*, 15.

(44) Blöchl, P. E. Projector Augmented-Wave Method. *Phys. Rev. B* **1994**, *50*, 17953.

(45) Pulay, P. *Ab Initio* Calculation of Force Constants and Equilibrium Geometries in Polyatomic Molecules: I. Theory. *Mol. Phys.* **1969**, *17*, 197.

(46) Heyd, J.; Scuseria, G. E.; Ernzerhof, M. Hybrid Functionals Based on a Screened Coulomb Potential. *J. Chem. Phys.* **2003**, *118*, 8207.

(47) Hartree, D. R. The Wave Mechanics of an Atom with a Non-Coulomb Central Field. Part I. Theory and Methods. *Math. Proc. Camb. Philos. Soc.* **1928**, *24*, 89.

(48) Fock, V. Näherungsmethode zur Lösung des Quantenmechanischen Mehrkörperproblems. *Z. Phys. A* **1930**, *61*, 126.

(49) Ganose, A. M.; Jackson, A. J.; Scanlon, D. O. sumo: Command-Line Tools for Plotting and Analysis of Periodic *ab Initio* Calculations. *J. Open Source Softw.* **2018**, *3*, 717.

(50) Jackson, A. J.; Ganose, A. M.; Regoutz, A.; Egdell, R. G.; Scanlon, D. O. Galore: Broadening and Weighting for Simulation of Photoelectron Spectroscopy. *J. Open Source Software* **2018**, *3*, 773.

(51) Madsen, G. K. H.; Singh, D. J. BoltzTraP. A Code for Calculating Band-Structure Dependent Quantities. *Comput. Phys. Commun.* **2006**, *175*, 67.

(52) Ganose, A. M.; Park, J.; Faghaninia, A.; Woods-Robinson, R.; Persson, K. A.; Jain, A. Efficient Calculation of Carrier Scattering Rates from First Principles. *Nat. Commun.* **2021**, *12*, 2222.

(53) Giustino, F.; Cohen, M. L.; Louie, S. G. Electron–Phonon Interaction using Wannier Functions. *Phys. Rev. B* **2007**, *76*, 165108.

(54) Togo, A.; Tanaka, I. First Principles Phonon Calculations in Materials Science. *Scr. Mater.* **2015**, *108*, 1.

(55) Togo, A.; Chaput, L.; Tanaka, I. Distributions of Phonon Lifetimes in Brillouin Zones. *Phys. Rev. B* **2015**, *91*, 094306.

(56) Skelton, J. M.; Tiana, D.; Parker, S. C.; Togo, A.; Tanaka, I.; Walsh, A. Influence of the Exchange–Correlation Functional on the Quasi-Harmonic Lattice Dynamics of II–VI Semiconductors. *J. Chem. Phys.* **2015**, *143*, 064710.

(57) Gonze, X.; Charlier, J.-C.; Allan, D. C.; Teter, M. P. Interatomic Force Constants from First Principles: The Case of α-Quartz. *Phys. Rev. B* **1994**, *50*, 13035.

(58) Lany, S.; Zunger, A. Assessment of Correction Methods for the Band-Gap Problem and for Finite-Size Effects in Supercell Defect Calculations: Case Studies for ZnO and GaAs. *Phys. Rev. B* **2008**, *78*, 17.

(59) Freysoldt, C.; Grabowski, B.; Hickel, T.; Neugebauer, J.; Kresse, G.; Janotti, A.; Van De Walle, C. G. First-Principles Calculations for Point Defects in Solids. *Rev. Mod. Phys.* **2014**, *86*, 253.

(60) Freysoldt, C.; Neugebauer, J.; Van de Walle, C. G. Fully *ab initio* Finite-Size Corrections for Charged-Defect Supercell Calculations. *Phys. Rev. Lett.* **2009**, *102*, 016402.

(61) Murphy, S. T.; Hine, N. D. M. Anisotropic Charge Screening and Supercell Size Convergence of Defect Formation Energies. *Phys. Rev. B* **2013**, *87*, 1.

(62) Buckeridge, J.; Jevdokimovs, D.; Catlow, C. R. A.; Sokol, A. A. Nonstoichiometry and Weyl Fermionic Behavior in TaAs. *Phys. Rev. B* **2016**, *94*, 180101.

(63) Buckeridge, J. Equilibrium Point Defect and Charge Carrier Concentrations in a Material Determined Through Calculation of the Self-Consistent Fermi Energy. *Computer Physics Communications* **2019**, *244*, 329.

(64) Taylor, F. H.; Buckeridge, J.; Catlow, C. R. A. Defects and Oxide Ion Migration in the Solid Oxide Fuel Cell Cathode Material $LaFeO_3$. *Chem. Mater.* **2016**, *28*, 8210.

(65) Buckeridge, J. SC-Fermi. https://github.com/jbuckeridge/sc-fermi, Accessed 28 February 2018.

(66) Pan, J.; Sun, Y.; Wan, P.; Wang, Z.; Liu, X. Preparation of $NaBiO_3$ and the Electrochemical Characteristic of Manganese Dioxide Doped with $NaBiO_3$. *Electrochim. Acta* **2006**, *51*, 3118.

(67) Bradley, C.; Cracknell, A. *The Mathematical Theory of Symmetry in Solids: Representation Theory for Point Groups and Space Groups*; Oxford University Press, 2009.

(68) Verhoeven, J. A. T.; Van Doveren, H. XPS Studies on Ba, BaO and the Oxidation of Ba. *Appl. Surf. Sci.* **1980**, *5*, 361.

(69) Uchida, K.; Ayame, A. Dynamic XPS Measurements on Bismuth Molybdate Surfaces. *Surf. Sci.* **1996**, *357*, 170.

(70) Nair, P. K.; Huang, L.; Nair, M. T. S.; Hu, H.; Meyers, E. A.; Zingaro, R. A. Formation of *p*-Type Cu_3BiS_3 Absorber Thin Films by Annealing Chemically Deposited Bi_2S_3–CuS Thin Films. *J. Mater. Res.* **1997**, *12*, 651.

(71) Schmidt, T. J.; Grgur, B. N.; Behm, R. J.; Markovic, N. M.; Ross Jr, P. N. Bi Adsorption on Pt (111) in Perchloric Acid Solution: A Rotating Ring–Disk Electrode and XPS Study. *Phys. Chem. Chem. Phys.* **2000**, *2*, 4379.

(72) Fan, H.; Wang, G.; Hu, L. Infrared, Raman and XPS Spectroscopic Studies of Bi_2O_3–B_2O_3–Ga_2O_3 Glasses. *Solid State Sci.* **2009**, *11*, 2065.

(73) Cao, J.; Xu, B.; Lin, H.; Luo, B.; Chen, S. Novel Heterostructured Bi_2S_3/BiOI Photocatalyst: Facile Preparation, Characterization and Visible Light Photocatalytic Performance. *Dalton Trans.* **2012**, *41*, 11482.

(74) Fu, J.; Song, S.; Zhang, X.; Cao, F.; Zhou, L.; Li, X.; Zhang, H. Bi_2Te_3 Nanoplates and Nanoflowers: Synthesized by Hydrothermal Process and Their Enhanced Thermoelectric Properties. *CrystEngComm* **2012**, *14*, 2159.

(75) Madhusudan, P.; Zhang, J.; Cheng, B.; Liu, G. Photocatalytic Degradation of Organic Dyes with Hierarchical $Bi_2O_2CO_3$ Microstructures Under Visible-Light. *CrystEngComm* **2013**, *15*, 231.

(76) Kubelka, P. Ein Beitrag zur Optik der Farbanstriche (Contribution to the Optic of Paint). *Z. Tech. Phys.* **1931**, *12*, 593.

(77) Dolgonos, A.; Mason, T. O.; Poeppelmeier, K. R. Direct Optical Band Gap Measurement in Polycrystalline Semiconductors: A Critical Look at the Tauc Method. *J. Solid State Chem.* **2016**, *240*, 43.

(78) Suemune, Y. Thermal Conductivity of $BaTiO_3$ and $SrTiO_3$ from 4.5 to 300 K. *J. Phys. Soc. Jpn.* **1965**, *20*, 174.

(79) He, J.; Hao, S.; Xia, Y.; Naghavi, S. S.; Ozoliņš, V.; Wolverton, C. Bi_2PdO_4: A Promising Thermoelectric Oxide with High Power Factor and Low Lattice Thermal Conductivity. *Chem. Mater.* **2017**, *29*, 2529.

(80) Takahata, K.; Iguchi, Y.; Tanaka, D.; Itoh, T.; Terasaki, I. Low Thermal Conductivity of the Layered Oxide (Na,Ca)Co_2O_4: Another Example of a Phonon Glass and an Electron Crystal. *Phys. Rev. B* **2000**, *61*, 12551.

(81) Spooner, K. B.; Einhorn, M.; Davies, D. W.; Scalon, D. O. ThermoPlotter. Online, 2021; https://github.com/SMTG-UCL/ThermoPlotter.

(82) Buckeridge, J.; Scanlon, D. O.; Walsh, A.; Catlow, C. R. A. Automated Procedure to Determine the Thermodynamic Stability of a Material and the Range of Chemical Potentials Necessary for its Formation Relative to Competing Phases and Compounds. *Comput. Phys. Commun.* **2014**, *185*, 330.

(83) Sallis, S.; Scanlon, D. O.; Chae, S. C.; Quackenbush, N. F.; Fischer, D. A.; Woicik, J. C.; Guo, J.-H.; Cheong, S.-W.; Piper, L. F. J. La-Doped $BaSnO_3$ — Degenerate Perovskite Transparent Conducting oxide: Evidence from Synchrotron X-Ray Spectroscopy. *Appl. Phys. Lett.* **2013**, *103*, 042105.

(84) Lebens-Higgins, Z.; Scanlon, D. O.; Paik, H.; Sallis, S.; Nie, Y.; Uchida, M.; Quackenbush, N. F.; Wahila, M. J.; Sterbinsky, G. E.; Arena, D. A.; Woicik, J. C.; Schlom, D. G.; Piper, L. F. J. Direct Observation of Electrostatically Driven Band Gap Renormalization in a Degenerate Perovskite Transparent Conducting Oxide. *Phys. Rev. Lett.* **2016**, *116*, 027602.

(85) Sokol, A. A.; French, S. A.; Bromley, S. T.; Catlow, C. R. A.; van Dam, H. J. J.; Sherwood, P. Point Defects in ZnO. *Faraday Discuss.* **2007**, *134*, 267.

(86) Scanlon, D. O.; Kehoe, A. B.; Watson, G. W.; Jones, M. O.; David, W. I. F.; Payne, D. J.; Egdell, R. G.; Edwards, P. P.; Walsh, A. Nature of the Band Gap and Origin of the Conductivity of PbO_2 Revealed by Theory and Experiment. *Phys. Rev. Lett.* **2011**, *107*, 246402.

(87) Varley, J. B.; Weber, J. R.; Janotti, A.; Van de Walle, C. G. Oxygen Vacancies and Donor Impurities in β-Ga_2O_3. *Appl. Phys. Lett.* **2010**, *97*, 142106.

(88) Ágoston, P.; Albe, K.; Nieminen, R. M.; Puska, M. J. Intrinsic *n*-Type Behavior in Transparent Conducting Oxides: A Comparative Hybrid-Functional Study of In_2O_3, SnO_2, and ZnO. *Phys. Rev. Lett.* **2009**, *103*, 245501.

(89) Limpijumnong, S.; Reunchan, P.; Janotti, A.; Van de Walle, C. G. Hydrogen Doping in Indium Oxide: An *ab Initio* Study. *Phys. Rev. B* **2009**, *80*, 193202.

(90) Buckeridge, J.; Catlow, C. R. A.; Farrow, M. R.; Logsdail, A. J.; Scanlon, D. O.; Keal, T. W.; Sherwood, P.; Woodley, S. M.; Sokol, A. A.; Walsh, A. Deep vs Shallow Nature of Oxygen Vacancies and Consequent *n*-Type Carrier Concentrations in Transparent Conducting Oxides. *Phys. Rev. Mater.* **2018**, *2*, 054604.

(91) Singh, A. K.; Janotti, A.; Scheffler, M.; Van de Walle, C. G. Sources of Electrical Conductivity in SnO_2. *Phys. Rev. Lett.* **2008**, *101*, 055502.

(92) Scanlon, D. O.; Watson, G. W. On the Possibility of p-Type SnO_2. *J. Mater. Chem.* **2012**, *22*, 25236.

(93) Kohan, A. F.; Ceder, G.; Morgan, D.; Van de Walle, C. G. First-Principles Study of Native Point Defects in ZnO. *Phys. Rev. B* **2000**, *61*, 15019.

(94) Lee, E.-C.; Kim, Y.-S.; Jin, Y.-G.; Chang, K.-J. Compensation Mechanism for N Acceptors in ZnO. *Phys. Rev. B* **2001**, *64*, 085120.

(95) Zhang, S. B.; Wei, S.-H.; Zunger, A. Intrinsic n-type Versus p-Type Doping Asymmetry and the Defect Physics of ZnO. *Phys. Rev. B* **2001**, *63*, 075205.

(96) Janotti, A.; Van de Walle, C. G. Oxygen Vacancies in ZnO. *Appl. Phys. Lett.* **2005**, *87*, 122102.

(97) Erhart, P.; Albe, K.; Klein, A. First-Principles Study of Intrinsic Point Defects in ZnO: Role of Band Structure, Volume Relaxation, and Finite-Size Effects. *Phys. Rev. B* **2006**, *73*, 205203.

(98) Janotti, A.; Van de Walle, C. G. Native Point Defects in ZnO. *Phys. Rev. B* **2007**, *76*, 165202.

(99) Lany, S.; Zunger, A. Dopability, Intrinsic Conductivity, and Nonstoichiometry of Transparent Conducting Oxides. *Phys. Rev. Lett.* **2007**, *98*, 045501.

(100) Oba, F.; Togo, A.; Tanaka, I.; Paier, J.; Kresse, G. Defect Energetics in ZnO: A Hybrid Hartree–Fock Density Functional Study. *Phys. Rev. B* **2008**, *77*, 245202.

(101) Muta, H.; Kurosaki, K.; Yamanaka, S. Thermoelectric Properties of Rare Earth Doped $SrTiO_3$. *J. Alloys Compd.* **2003**, *350*, 292.

(102) Obara, H.; Yamamoto, A.; Lee, C.-H.; Kobayashi, K.; Matsumoto, A.; Funahashi, R. Thermoelectric Properties of Y-Doped Polycrystalline $SrTiO_3$. *Jpn. J. Appl. Phys.* **2004**, *43*, L540.

(103) Muta, H.; Kurosaki, K.; Yamanaka, S. Thermoelectric Properties of Doped $BaTiO_3$–$SrTiO_3$ Solid Solution. *J. Alloys Compd.* **2004**, *368*, 22.

(104) Muta, H.; Kurosaki, K.; Yamanaka, S. Thermoelectric Properties of Reduced and La-Doped Single-Crystalline $SrTiO_3$. *J. Alloys Compd.* **2005**, *392*, 306.

(105) Yamada, Y. F.; Ohtomo, A.; Kawasaki, M. Parallel Syntheses and Thermoelectric Properties of Ce-Doped $SrTiO_3$ Thin Films. *Appl. Surf. Sci.* **2007**, *254*, 768.

(106) Pei, Y.-L.; Liu, Y. Electrical and Thermal Transport Properties of Pb-Based Chalcogenides: PbTe, PbSe, and PbS. *J. Alloys Compd.* **2012**, *514*, 40.

(107) Qiu, B.; Bao, H.; Ruan, X.; Zhang, G.; Wu, Y. Molecular Dynamics Simulations of Lattice Thermal Conductivity and Spectral Phonon Mean Free Path of PbTe: Bulk and Nanostructures. Proceedings of the ASME 2012 Heat Transfer Summer Conference. 2012; p 659.